Characterizing Hydrated Sulfates and Altered Phases in Jezero Crater Fan and Floor Geologic Units With SHERLOC on Mars 2020

Yu Yu Phua, Bethany L. Ehlmann, Sandra Siljeström, Andrew D. Czaja, Pierre Beck, Stephanie Connell, Roger C. Wiens, Ryan S. Jakubek, Rebecca M. E. Williams, Maria-Paz Zorzano, et al.

JGR Planets

RESEARCH ARTICLE
10.1029/2023JE008251

Special Collection:
The Perseverance Rover's Exploration of the Western Fan Front, Jezero Crater, Mars

Characterizing Hydrated Sulfates and Altered Phases in Jezero Crater Fan and Floor Geologic Units With SHERLOC on Mars 2020

Yu Yu Phua[1], Bethany L. Ehlmann[1], Sandra Siljeström[2], Andrew D. Czaja[3], Pierre Beck[4], Stephanie Connell[5], Roger C. Wiens[5], Ryan S. Jakubek[6], Rebecca M. E. Williams[7], Maria-Paz Zorzano[8], Michelle E. Minitti[9], Alyssa C. Pascuzzo[10], Kevin P. Hand[11], Rohit Bhartia[12], Linda C. Kah[13], Lucia Mandon[1], Joseph Razzell Hollis[14], Eva L. Scheller[15], Sunanda Sharma[11], Andrew Steele[16], Kyle Uckert[11], Kenneth H. Williford[17], and Anastasia G. Yanchilina[1]

[1]Division of Geological and Planetary Sciences, California Institute of Technology, Pasadena, CA, USA, [2]RISE Research Institutes of Sweden, Stockholm, Sweden, [3]Department of Geosciences, University of Cincinnati, Cincinnati, OH, USA, [4]CNRS-IPAG, Université Grenoble Alpes, Grenoble, France, [5]Earth, Atmospheric, and Planetary Sciences, Purdue University, West Lafayette, IN, USA, [6]Jacobs, NASA Johnson Space Center, Houston, TX, USA, [7]Planetary Science Institute, Tucson, AZ, USA, [8]Centro de Astrobiología (CAB), CSIC-INTA, Madrid, Spain, [9]Framework, Silver Spring, MD, USA, [10]Malin Space Science Systems, San Diego, CA, USA, [11]Jet Propulsion Laboratory, California Institute of Technology, Pasadena, CA, USA, [12]Photon Systems Inc., Covina, CA, USA, [13]Department of Earth and Planetary Sciences, University of Tennessee, Knoxville, TN, USA, [14]The Natural History Museum, London, UK, [15]Department of Earth, Atmospheric, and Planetary Sciences, MIT, Cambridge, MA, USA, [16]Carnegie Institution of Washington, Washington, DC, USA, [17]Blue Marble Space Institute of Science, Seattle, WA, USA

Key Points:

- $MgSO_4{\cdot}nH_2O$ ($2 < n \leq 5$) are found in the Jezero fan and floor while low-hydration $MgSO_4{\cdot}nH_2O$ (n = 1–2) are more commonly found in the fan
- Hydrated Ca-sulfates are found only in the upper fan
- The diverse phases imply salt formation from high ionic strength fluids and subsequent aridity to preserve the observed hydration states

Correspondence to:
Y. Y. Phua,
yphua@caltech.edu

Citation:
Phua, Y. Y., Ehlmann, B. L., Siljeström, S., Czaja, A. D., Beck, P., Connell, S., et al. (2024). Characterizing hydrated sulfates and altered phases in Jezero Crater fan and floor geologic units with SHERLOC on Mars 2020. *Journal of Geophysical Research: Planets*, *129*, e2023JE008251. https://doi.org/10.1029/2023JE008251

Received 17 DEC 2023
Accepted 13 APR 2024

Abstract

The Mars 2020 Perseverance rover has explored fluvio-lacustrine sedimentary rocks within Jezero crater. Prior work showed that igneous crater floor Séítah and Máaz formations have mafic mineralogy with alteration phases that indicate multiple episodes of aqueous alteration. In this work, we extend the analyses of hydration to targets in the Jezero western fan delta, using data from the SHERLOC (Scanning Habitable Environments with Raman and Luminescence for Organics and Chemicals) Raman spectrometer. Spectral features, for example, sulfate and hydration peak positions and shapes, vary within, and across the crater floor and western fan. The proportion of targets with hydration associated with sulfates was approximately equal in the crater floor and the western fan. All hydrated targets in the crater floor and upper fan showed bimodal hydration peaks at ~3,200 and ~3,400 cm^{-1}. The sulfate symmetric stretch at ~1,000 cm^{-1} coupled with a hydration peak at ~3,400 cm^{-1} indicate that $MgSO_4{\cdot}nH_2O$ ($2 < n \leq 5$) is a likely hydration carrier phase in all units, perhaps paired with low-hydration ($n \leq 1$) amorphous Mg-sulfates, indicated by the ~3,200 cm^{-1} peak. Low-hydration $MgSO_4{\cdot}nH_2O$ (n = 1–2) are more prevalent in the fan, and hydrated targets in the fan front only had one peak at ~3,400 cm^{-1}. While anhydrite co-occurs with hydrated Mg-sulfates in the crater floor and fan front, hydrated Ca-sulfates are observed instead at the top of the upper fan. Collectively, the data imply aqueous deposition of sediments with formation of salts from high ionic strength fluids and subsequent aridity to preserve the observed hydration states.

Plain Language Summary

The Mars 2020 Perseverance rover has explored a fan delta deposit in the Jezero crater where a lake was present in the past. In this work, we use the SHERLOC (Scanning Habitable Environments with Raman and Luminescence for Organics and Chemicals) Raman spectroscopy instrument on the rover to determine the minerals that contain water in the form of H_2O and/or OH. These hydrated minerals are indicators of interactions of rock with water and inform us how the environmental conditions and the habitability of Jezero crater evolved over time. Hydrated Mg-sulfates $MgSO_4{\cdot}nH_2O$ ($2 < n \leq 5$) are observed in both the crater floor and the western fan. Mg-sulfates of lower hydration degree (n = 1–2) are more commonly found in the western fan, particularly the fan front. Hydrated Ca-sulfate is found only close to the top of the fan. These changes in sulfate degree of hydration and/or cations from the floor to the fan are evidence of multiple past fluid events and chemistries at Jezero crater.

1. Introduction

The long- and short-timescale processes recorded by hydrated minerals help us understand how the climate and consequently the habitability of a planet evolve over time. The hydrated minerals as they appear today inform us about modern, short-timescale processes of present-day exchange with the atmosphere such as changes in hydration states of salts as a function of relative humidity (RH) (e.g., Vaniman & Chipera, 2006). Hydrated minerals also record the early Martian climate. Orbital detections of the occurrences of phyllosilicates in Noachian and early Hesperian terrains (>3.5 Ga), salts and silica largely in Hesperian terrain (~3–3.5 Ga), and negligible hydrous minerals in Amazonian terrain (~3 Ga to present day) imply large-scale shifting climatic conditions over time from early wetter periods to the present-day cold and dry conditions (e.g., Bibring et al., 2006; Murchie et al., 2009). However, landed in situ investigations showed formation of phyllosilicate into the Early Hesperian period at Gale crater (e.g., Bristow et al., 2018), pointing to the fact that there are complex aqueous environments and histories at the local scale not captured by orbital detections.

The nature of interaction with water over time, including the intensity, duration, and style of alteration the rock has experienced are open questions at most locations on Mars. In a few locations across the planet, these can be answered through in situ measurements of the abundance and hydration states of Martian hydrated minerals from landed missions. The lateral measurement resolution, via mobility and remote sensing, and vertical resolution to the shallow subsurface, offered by landed in situ investigations, have been useful in constraining the water content (H_2O and/or OH) of Mars' rocks and the hydration carrier phases. The estimated bulk water contents of rocks at the different landing sites of the Opportunity, Spirit, and Curiosity rovers range from ~1 wt.% for typical rocks to ~20 wt.% for highly altered rocks. Except for jarosite, the hydration states of the sulfates as well as the mineralogy of secondary silicate phases were not constrained by direct measurements from the Spirit or Opportunity rovers. Estimates of the water content were instead made based on models including Fe^{3+}-, Mg-, and Ca-bearing sulfates of different hydration states such as paracoquimbite, gypsum, kieserite and epsomite. For example, the most hydrated rocks at Meridiani Planum were modeled to contain 6-22 wt.% water, hypothesized to be carried by hydrated minerals such as Mg-sulfates, Ca-sulfates and jarosite (B. C. Clark et al., 2005). At Gusev crater, a notable hydrated target was the Paso Robles soil, with up to 17 wt.% water believed to be associated with Fe^{3+}-, Mg-, and Ca-bearing sulfates (Campbell et al., 2008). In contrast, X-ray diffraction measurements by CheMin at Gale crater provided specific mineral identifications of alteration minerals and the carrier phases of hydration, including Ca-sulfates (gypsum, bassanite, anhydrite), Mg-sulfates (kieserite, starkeyite), the Fe-sulfate group mineral jarosite, dioctahedral and trioctahedral Fe/Mg-smectites, and Fe-carbonate siderite (Chipera et al., 2023; Rampe et al., 2017, 2020; Thorpe et al., 2022; Vaniman et al., 2014, 2018). The X-ray amorphous phase(s) detected at Gale crater also appear to be hydrated (Chipera et al., 2023). Lacustrine sedimentary rocks containing hydrated sulfates, phyllosilicates, hydrated silica, and oxyhydroxides at Gale crater were found to typically have abundance of ~2–3 wt.% water with as much as 18 wt.% water in some samples enriched in hydrated phases (Rapin et al., 2018; Sutter et al., 2017; Thomas et al., 2020). The wide range of alteration phases at these landing sites indicates that the different locations have experienced different aqueous environments.

Most recently, the Mars 2020 Perseverance rover has been exploring the Noachian-aged Jezero crater to analyze the chemistry, mineralogy and texture at outcrop- to sub-millimeter scales in order to understand the origins and history of the Jezero crater rocks, search for biosignatures, and collect samples for return to Earth (Farley et al., 2020). Based on orbital data, Jezero crater is hypothesized to formerly host a lake, similar to Gusev and Gale craters. Jezero crater has two inlet valleys, one outlet valley, and a northern and western depositional fan delta (hereafter, we use "fan" to refer to the fan delta) as well as a volcanic floor (Fassett & Head, 2005; Goudge et al., 2015). Orbital spectroscopic observations have shown alteration and hydrated phases inside Jezero crater and in its associated watershed (Ehlmann et al., 2008, 2009; Goudge et al., 2015; Horgan et al., 2020). Fe/Mg-smectite and Mg-rich carbonate have been detected in the watershed, which are interpreted to be one possible source for the Fe/Mg-smectite and Mg-rich carbonate in the western fan and margin deposits. Hydrated silica has also been detected near the western fan (Tarnas et al., 2019). The occurrences of smectite, carbonate, and hydrated silica suggest a close-to-neutral fluid environment in Jezero crater during their formations (Ehlmann et al., 2008, 2009; Tarnas et al., 2019). However, the relationship between fluvial activity in the Jezero crater ancient lake and the formation of alteration phases is unclear.

The Mars 2020 rover has thus far explored the igneous crater floor units Séítah and Máaz, followed by sedimentary rocks of the western fan. Prior work on the crater floor showed that Séítah and Máaz have a dominantly

primary igneous mineralogy. Alteration phases such as sulfates, carbonates, phyllosilicates, and oxyhydroxides were also detected (e.g., Corpolongo et al., 2023; Farley et al., 2022; Mandon et al., 2023; Scheller et al., 2022; Tice et al., 2022; Wiens et al., 2022). The similarity of the cation composition of the Fe/Mg-carbonate to olivine in Séítah and Máaz suggests the carbonate was formed from the alteration of olivine, but the preservation of olivine grains implies limited fluid availability (Clavé et al., 2023; Siljeström et al., 2024; Tice et al., 2022). The in situ detections of highly soluble sulfate and perchlorate phases in the pore spaces of rocks not seen from orbit indicate there was a later period of aqueous activity after the formation of phyllosilicates. This later episode(s) of aqueous activity precipitated sulfate and/or perchlorate from a brine distinct in composition from the earlier fluid that formed the carbonate, based on the lack of correlation of the Fe/Mg cation composition of the sulfate and the olivine (Siljeström et al., 2024; Tice et al., 2022). These assemblages of minerals indicate that there were diverse aqueous environments in Jezero crater in the past.

In this work, we extend the analyses of Siljeström et al. (2024), which reported hydration on the crater floor based on data from the Scanning Habitable Environments with Raman and Luminescence for Organics and Chemicals (SHERLOC) instrument. Based on analyses of the SHERLOC Raman spectral parameters combined with the Planetary Instrument for X-ray Lithochemistry (PIXL) data, Siljeström et al. (2024) have suggested that crystalline/amorphous Mg-sulfate with 3–5 waters per formula unit and low-hydration $MgSO_4{\cdot}H_2O$ are present in the igneous crater floor. Here, we characterize the alteration mineralogy and hydration carrier phases of sedimentary rock targets in the Jezero western fan and compare these results with the igneous crater floor units.

We conduct a statistical analysis of the deep-UV Raman spectra of all stratigraphically in-place rock targets measured by SHERLOC at the Séítah and Máaz formations of the crater floor, the fan front (informally named the Shenandoah formation, Stack et al., 2024), and the upper fan deposits (informally named the Tenby formation, e.g., Siebach et al., 2023) of the sedimentary western fan. We first analyze Raman spectral features in SHERLOC scans at 100 μm/point spatial scale over 800–1,200 cm^{-1} to identify the alteration minerals present. We then examine the details of the positions and shapes of corresponding Raman spectroscopic features in the 2,800–3,900 cm^{-1} hydration-related spectral region, where the stretching modes of both molecular H_2O and structural OH are observed, to determine the hydration state by comparison to terrestrial laboratory data. We compare these results with SuperCam's near-infrared reflectance spectrometer (IRS) hydration data from the ∼1.9-μm absorption caused by the bending and stretching modes in molecular H_2O and with the 656-nm hydrogen peak observed in laser-induced breakdown spectra (LIBS) obtained from the same targets. We then consider variability within and between targets, relating to the geologic units, to understand whether/how the fluid environments changed across time and space in the Jezero crater system.

2. Methods

2.1. SHERLOC Spectrometer and Targets Analyzed

SHERLOC is an arm-mounted Raman and fluorescence spectroscopy and context imaging proximity science instrument with a 248.6 nm NeCu deep-ultraviolet (DUV) pulsed laser excitation source (40 μs pulse width), which analyzes the mineralogy correlated to textural features at a high spatial resolution of 100 μm (Bhartia et al., 2021). The incident laser is moved point-by-point in a grid to generate a two-dimensional scan of Raman and fluorescence spectra with up to 1,296 individual points within a 7 × 7 mm area depending on the types of scans. The scan types analyzed in this work are “High Dynamic Range” (HDR; scan area 7 × 7 mm, step size 780 μm) and “detail” (scan area 1 × 1 mm, step size 100 μm), both consisting of 100 points in a 10 × 10 grid.

SHERLOC has a working distance of ∼48 mm to the surface of the target and analyzes both abraded targets and natural surfaces. Abraded patches are nominally 50 mm in diameter and 7–10 mm deep with a relatively flat surface that is cleaned of dust by the gaseous dust removal tool (gDRT) following abrasion (Moeller et al., 2021). Natural surfaces are not abraded but are sometimes partially cleaned of dust by the gDRT or with the shock waves from LIBS laser pulses (labeled as LIBS cleared in Table 1). The rover explored the igneous crater floor (up to sol 380), the sedimentary western fan front known as the Shenandoah formation (Stack et al., 2024; sol 414 to sol 707), and the upper fan named the Tenby formation (e.g., Siebach et al., 2023; sol 708 to sol 912). We analyzed all SHERLOC Raman data acquired with at least 100 laser pulses per point (ppp) for bedrock targets from four regions: the Séítah formation, the Máaz formation, the sedimentary western fan front, and the upper fan (Table 1 for list of targets; Figure 1 for locations of SHERLOC scan targets; Figure 2 for footprints of SHERLOC scans). SHERLOC scans up to sol 161 (target names Nataani, Bi La Sana, Foux, and Guillaumes on sol 161) were

Table 1
List of SHERLOC Targets Analyzed in This Work

Target name	Abrasion performed on sol	SHERLOC spectroscopy obtained on sol	SHERLOC spectroscopy start time (LMST)	Scan types obtained (laser pulses per point)
Séítah				
Garde	206	207	20:19	HDR ×2 (500/500)
		208	19:37	Detail ×3 (500/500/500)
Dourbes	253	257	20:03	HDR ×1 (500)
		269	19:50	Detail ×3 (500/500/500)
Quartier	292	293	20:01	HDR ×1 (500)
		304	21:01	Detail ×4 (500/500/500/500)
Máaz				
Nataan	Natural (LIBS-cleared)	83	12:18	HDR ×1 (100)
Bi La Sana	Natural	98	11:27	HDR ×3 (100/100/300)
Foux	Natural (LIBS-cleared)	141	12:21	HDR ×3 (100/100/300)
Guillaumes	160	161	16:28	HDR ×3 (100/100/300)
		162	19:58	HDR ×2 (250/250)
Bellegarde	185	186	18:55	HDR ×2 (250/250)
Montpezat	346	349	20:04	HDR ×1 (500)
Fan front (Shenandoah)				
Pignut Mountain	Natural (LIBS-cleared)	463	20:19	HDR ×1 (500)
Shop Hollow	Natural	480	20:02	HDR ×1 (500)
Thornton Gap	482	489	19:31	HDR ×2 (500/500)
				Detail ×2 (500/500)
Berry Hollow	504	505	18:45	HDR ×1 (500)
				Detail ×1 (500)
		513	20:50	Detail ×4 (500/500/500/500)
Chiniak	Natural (LIBS-cleared)	558	18:51	Detail ×1 (500)
Novarupta	Natural (LIBS-cleared)	567	18:32	HDR ×1 (500)
	568	570	19:19	HDR ×1 (500)
		573	19:51	Detail ×2 (500/500)
Uganik Island	612	614	19:32	HDR ×1 (500)
				Detail ×2 (500/500)
		617	19:09	HDR ×1 (500)
				Detail ×2 (500/500)
		618	19:30	Detail ×2 (900/500)
		620	19:32	Detail ×2 (900/500)
Utz Gap	Natural (gDRT-cleared)	697	21:03	Detail ×4 (500/500/500/500)
Upper fan (Tenby)				
Solva	742	747	20:15	Detail ×2 (500/500)
		751	20:42	Detail ×2 (900/900)
Pipit Lake	Natural (gDRT-cleared)	781	20:11	Detail ×1 (500)
Solitude Lake	777	782	19:51	Detail ×2 (500/500)
Ouzel Falls	788	789	20:04	Detail ×1 (500)
		790	19:58	Detail ×2 (900/900)
		810	19:37	Detail ×2 (500/500)
Pilot Mountain	Natural (gDRT-cleared)	874	20:47	Detail ×1 (500)

Table 1
Continued

Target name	Abrasion performed on sol	SHERLOC spectroscopy obtained on sol	SHERLOC spectroscopy start time (LMST)	Scan types obtained (laser pulses per point)
Gabletop Mountain	877	879	20:01	Detail ×4 (500/500/500/500)
Thunderbolt Peak	Natural (gDRT-cleared)	888	20:16	Detail ×1 (500)
	893	894	20:29	Detail ×2 (500/500)

acquired during daytime with the RH <2% and temperature ~241 K but all subsequent SHERLOC scans were acquired after sunset on Mars (Table 1), with the RH ~<3% and temperature ~200–220 K (Polkko et al., 2023; Siljeström et al., 2024).

2.2. SHERLOC Spectrometer Characteristics That Affect Observed Mineral and Hydration Peaks

In general, Raman signal intensity depends on sample properties including crystallinity, crystal orientation, grain size, transparency of the mineral to both incident and scattered radiation, Raman scattering cross-section of the mineral, and roughness of the surface. Changes in crystal orientation with respect to incident light polarization can result in a change in relative Raman band intensities. Specific to SHERLOC, for each pulse, the SHERLOC laser produces two overlapping annular-shaped beams (Razzell Hollis et al., 2020) each with a different polarization for each pulse. The SHERLOC spectra examined in this work utilize 100–900 pulses per spectrum. This results in each SHERLOC Raman spectrum being an average of different relative crystal-polarization orientations. As a result, SHERLOC spectra will have minimal to negligible crystal orientation effects.

Additional characteristics specific to SHERLOC influence observed peak intensities for specific types of targets. Fe^{3+} cations are strongly absorbing at the wavelength of the SHERLOC deep-UV laser excitation source (248.6 nm), making it challenging to detect Fe^{3+}-bearing phases with SHERLOC, including Fe^{3+}-bearing oxides, oxyhydroxides, and phyllosilicates. Fe^{3+} cations in nanophase ferric oxide and magnetite are also major components of dust on the Mars surface (Lichtenberg et al., 2007; Morris et al., 2006), so SHERLOC is better able to detect Raman signals from dust-cleared abraded patches than natural surfaces that are incompletely cleared of dust.

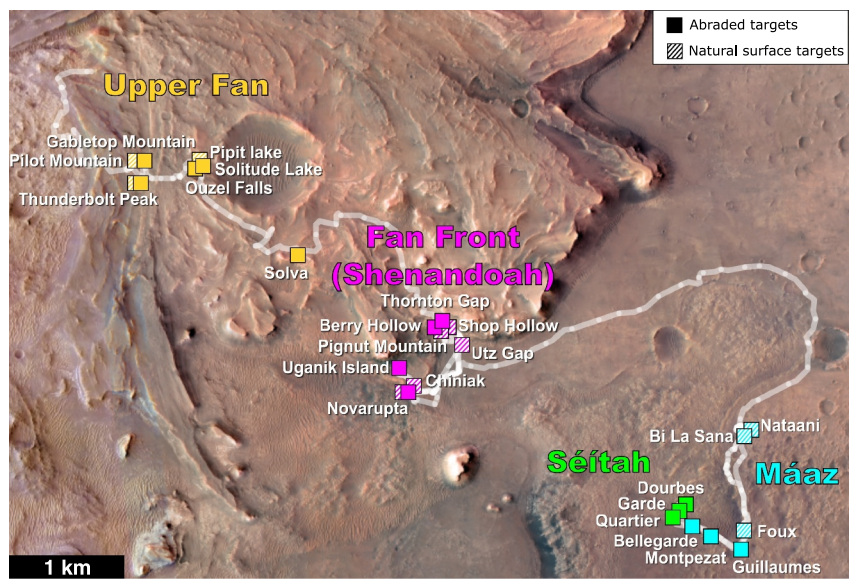

Figure 1. Locations of all SHERLOC bedrock targets analyzed in this work from the four regions: the Séítah formation, the Máaz formation, the sedimentary western fan front (Shenandoah formation), and the upper fan.

10.1029/2023JE008251

Figure 2. The footprints of SHERLOC scans for the (a) abraded targets and (b) natural surface targets analyzed in this work. The images were acquired with the Autofocus Context Imager (ACI) at grayscale as in (b), and colorized by overlaying RGB color images taken by the Wide Angle Topographic Sensor for Operations and Engineering (WATSON) camera (Sharma et al., 2023) for abraded targets in (a) at daytime in full shadow, unless otherwise specified in the images. Textural features mentioned in Table 3 are marked with arrows.

The effective Raman spectral region on SHERLOC is ~800–4,000 cm^{-1} because SHERLOC optics have an edge filter that attenuates signals at <600 cm^{-1}. There is also a secondary laser emission line at ~650 cm^{-1} that may interfere with Raman peaks in this region; signals from phases need to be of high intensity to be observed at <800 cm^{-1}. Mineral peaks are found in the ~800–1,200 cm^{-1} range, and previous SHERLOC analyses of this region have detected primary phases such as olivine and pyroxene, as well as alteration phases such as sulfate, carbonate, perchlorate and phosphate in the crater floor igneous rocks (Corpolongo et al., 2023; Scheller et al., 2022). Other groups of silicates such as plagioclase feldspar have not been definitively identified so far because of the low Raman scattering cross-sections of silicates compared to sulfates and carbonates. Feldspar in particular has a smaller cross-section than olivine and pyroxene (Haskin et al., 1997; Qi et al., 2023). The detection of feldspar as well as other silicates such as phyllosilicates and amphiboles with SHERLOC is further made difficult because the prominent Raman peaks of many silicates including feldspar, phyllosilicate, and amphibole are found <800 cm^{-1}.

2.3. Raman Peaks of Interest for Mineral Hydration State

Hydration bands originating from the O-H symmetric and asymmetric stretching modes of both molecular H_2O and structural OH are found in the ~3,000–4,000 cm^{-1} range. The O-H stretching modes due to molecular H_2O or structural OH can sometimes be distinguished with Raman spectroscopy methods based on the peak position and peak width. Structural OH groups that are coordinated with other cations occupy well-defined crystallographic sites in a mineral and often produce sharp peaks at >3,600 cm^{-1}. Molecular H_2O can sometimes occupy a well-defined crystallographic site, such as in gypsum or in open internal spaces such as the interlayer H_2O in phyllosilicates. However, due to the variability of the electronic field surrounding the H_2O molecules in the crystal structure in both cases, the hydrogen bond lengths are variable (Santos et al., 2018), resulting in broader bands at lower energy (3,000–3,600 cm^{-1}) for H_2O molecules relative to structural OH peaks (Chio et al., 2004). These broad molecular H_2O bands, associated with hydrated sulfates, were detected in the crater floor with SHERLOC (Siljeström et al., 2024). For interlayer H_2O in phyllosilicates, the non-defined sites of molecular H_2O further result in variable peak positions and intensities (Wang et al., 2015). Features in the 800–1,200 cm^{-1} Raman region and their peak positions can influence the shape and position of hydration features in the ~3,000–4,000 cm^{-1} region and are used to further constrain hydrated phases.

2.4. Data Processing Procedure

Each SHERLOC scan involves first acquiring a dark spectrum without the laser firing, and subsequently an active spectrum with the laser enabled. All SHERLOC Raman spectra reported here represent the active spectrum with the dark spectrum subtracted to account for the dark current. The spectral resolution of the SHERLOC spectrometer in the 400–4,000 cm^{-1} Raman region is 10.49 cm^{-1}/pixel (Razzell Hollis et al., 2021). Prior to peak fitting, the median spectrum of the instrument flat field signal obtained on Sol 413 for HDR scans and Sol 670 for detail scans was subtracted from each target's [active-dark] spectrum to correct for signals from the instrument's optics, some from fused silica. The instrument flat field signal was obtained by firing the laser at night when the robotic arm was stowed and the cover is open, so that no target was in focus.

The shape of a band as observed on an output spectrum is a result of the convolution of the intrinsic Raman band (i.e., the Raman response of a material that will be obtained if a spectrometer had infinitely high resolution) and the spectral response of the spectrometer. The intrinsic Raman bands of well-ordered crystalline solids are generally homogeneously broadened (Califano & Schettino, 1988; Mukamel, 1985), are likely Lorentzian and have full width at half-maximum (FWHM) < 50 cm^{-1}. In the SHERLOC Raman spectra, the observed band shapes of peaks of FWHM up to ~50 cm^{-1} are largely dominated by the SHERLOC instrument slit function, which is well-approximated as a Gaussian (Jakubek et al., 2023). On the other hand, for amorphous solids and hydration bands in the ~3,000–4,000 cm^{-1} region, the intrinsic Raman bands are generally inhomogeneously broadened due to the diversity of microenvironments (Leikin et al., 1997; Walrafen et al., 1996), giving rise to Gaussian band shapes. The convolution of a Gaussian intrinsic Raman band with a Gaussian SHERLOC instrument slit function creates an observed Raman band that is Gaussian. Both crystalline and amorphous mineral Raman peaks in the 800–1,200 cm^{-1} region, and hydration Raman bands in the ~3,000–4,000 cm^{-1} region from the SHERLOC Raman spectra can thus be approximated with Gaussian profiles, and we fit peaks with a 1D Gaussian profile.

The uncertainty of the peak position is estimated using Equation 1 in Lenz and Ayres (1992). For a peak in the SHERLOC Raman spectrum with signal-to-noise ratio (SNR) = 2 (which is the peak detection threshold we have used; see Section 2.5), full-width at half-maximum (FWHM) = 30 cm^{-1} and sampling interval = 9 cm^{-1}, the uncertainty of the peak position is ~5.7 cm^{-1}. As described by Fries et al. (2022), the error in the SHERLOC wavenumber calibration is ±1.8 cm^{-1}. This error in wavenumber calibration combined with the ~±5.7 cm^{-1} error associated with peak fitting for a band with SNR = 2 results in a peak position error of ~7.5 cm^{-1}. The uncertainty of the peak position is inversely proportional to SNR and will decrease for higher SNR, to ~2.9 cm^{-1} for SNR = 10.

All SHERLOC Raman spectra Gaussian fitting was performed using the SciPy library of Python (Virtanen et al., 2020). Up to three Gaussian components with a constant baseline were used to model the 800–1,200 cm^{-1} region (hereafter, "the mineral region"), where diagnostic peaks of minerals such as sulfate and carbonate are found. Cosmic ray spikes were not removed in the mineral region because of the difficulties of differentiating between cosmic ray spikes and mineral peaks that are also narrow and can be highly intense. Potential cosmic ray spikes were filtered by setting a threshold for the FWHM, which is described in Section 2.5. The 2,800–3,900 cm^{-1} region (hereafter, "the hydration region") was fit separately, with peak positions limited to 3,000–3,700 cm^{-1}, where hydration peaks are observed. The model in the hydration region allowed up to two Gaussian peak fits with a linear baseline used to approximate and offset the effects of fluorescence extending into this region, which is observed in some spectra. However, a linear model does not perfectly model the baseline, which is variable from point-to-point and sometimes has minor curvature. Incomplete removal of the baseline by underfitting a linear model could cause the baseline curvature to be fit as peaks, potentially creating false positives of hydration detections, but we have selected our SNR thresholds to largely avoid this effect (see Section 2.5). More work is needed to best-model the baseline of SHERLOC Raman spectra.

2.5. Peak Detection Thresholds

Fitted peaks of lower confidence were filtered and removed in subsequent analyses, based on two peak detection criteria. The first peak detection criterion is based on a comparison of the peak intensity to the noise standard deviation. In this work, we define the SNR as the intensity of the fitted peak divided by the standard deviation of noise across 2,000–2,100 cm^{-1}, a region where no Raman peaks are present. The SNR threshold in this work was set as >2× the noise standard deviation, providing a >95% certainty that an intensity is produced by signal. This threshold was set based on the observation that there are two kinds of peaks in the SHERLOC Raman spectra: peaks that are broad (FWHM >~100 cm^{-1}) and of lower intensities such as the hydration peaks, and peaks that are narrow (FWHM ~20–30 cm^{-1}) and of higher intensities, which include most mineral peaks, such as sulfates and carbonates (Figure 3). Both types of peaks are significant, so the threshold was set to SNR > 2 to retain broad peaks as real detections. In Figures 4 and 5, peaks are classified by color to signify thresholds. Alternative approaches to calculate the SNR and results sensitivity are described in Appendix A.

The second peak detection criterion is based on the FWHM of the fitted peaks. In the mineral region, a lower bound to the FWHM was set at 20 cm^{-1} (~2 spectral detection elements) to separate mineral signals from potential cosmic ray spikes. A SHERLOC Raman peak cannot be narrower than the 34.1 cm^{-1} FWHM of the slit function, and a feature with a FWHM <34.1 cm^{-1} is likely a cosmic ray or anomalous pixel feature (Jakubek et al., 2023). However, there is some error associated with band width value measurements that can report a FWHM <34.1 cm^{-1} for a Raman peak, thus a FWHM lower limit of 20 cm^{-1} was used to avoid the removal of these Raman peaks from consideration. An upper bound was set at 100 cm^{-1}. This is approximately 1.5× the maximum FWHM reported by Siljeström et al. (2024) attributed to amorphous sulfate peaks, which tend to have broader peaks than crystalline materials. Peaks outside of these bounds were not considered in subsequent analyses. The peak detection methods in this work are optimized to detect mineral peaks of alteration phases, and are not optimized for silicate peaks described by Corpolongo et al. (2023) and Scheller et al. (2022) that have large FWHM of >100 cm^{-1}.

In the hydration region where peaks are visibly broad, the lower bound was set at greater than 50 cm^{-1} to reduce false positives of peaks fitted to higher frequency noise. An upper bound to the FWHM was also set to avoid capturing the broad changes in the continuum and to isolate hydration features specifically. The upper bound of 300 cm^{-1} was chosen based on the observation that some hydrous sulfates such as kieserite, as measured in the laboratory, show broad hydration bands of FWHM ~300 cm^{-1}.

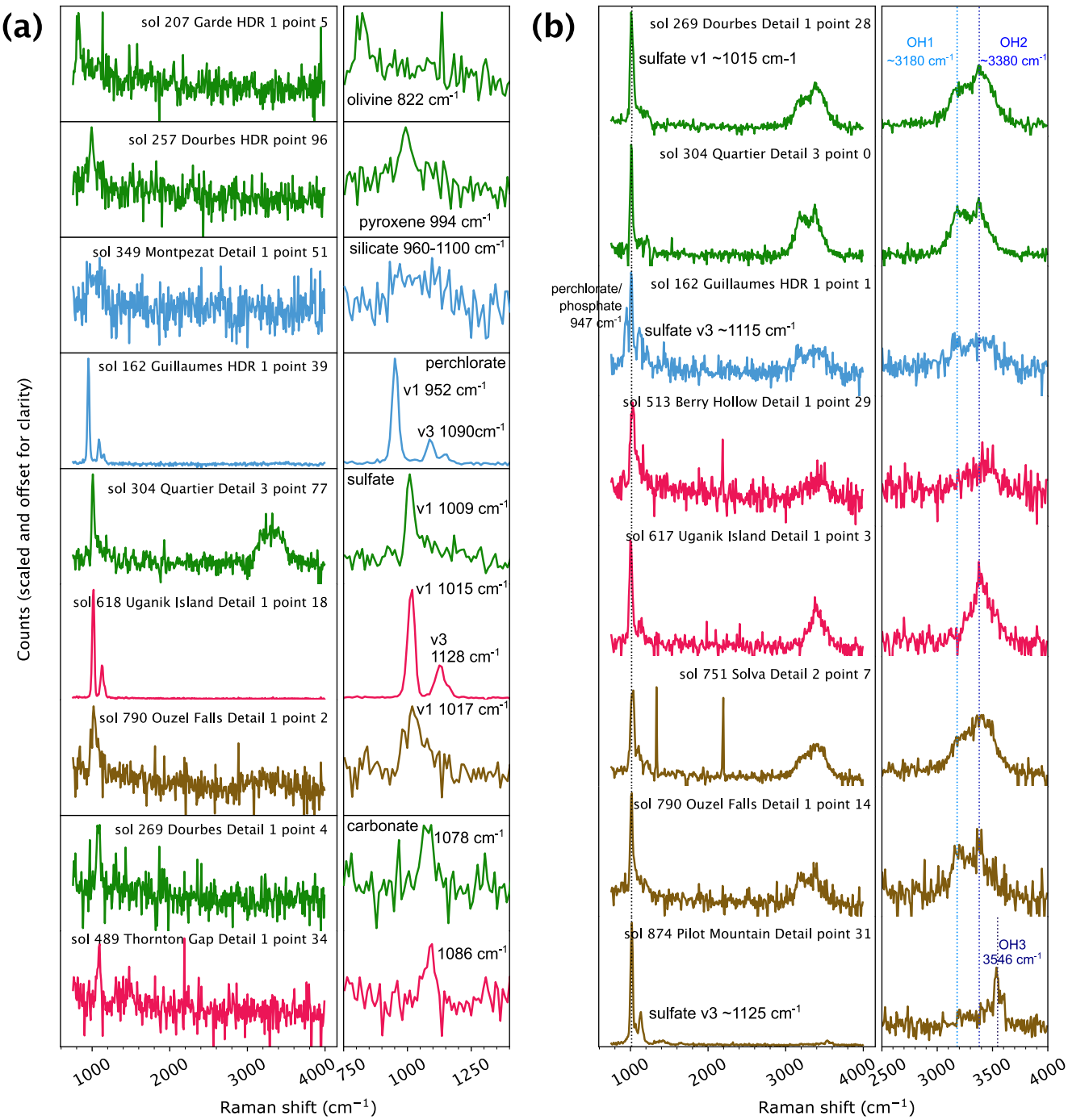

Figure 3. Example spectra from various abraded targets, colored by units (green: Séítah, blue: Máaz, pink: fan front, brown: upper fan) showing detections of (a) primary phases olivine, pyroxene and silicate, and alteration phases perchlorate, sulfate, and carbonate, and (b) hydration associated with sulfate phases. Vertical dashed lines indicate peak positions of sulfate ν_1 symmetric stretch mode and hydration detections, with OH1, OH2, OH3 indicating successively higher wavenumber hydration peaks at ~3,180, ~3,380, and ~3,550 cm^{-1}, respectively.

2.6. Comparison With Laboratory Data for Mineral Phase Identification

Mineral identification was done by comparing the peak positions of SHERLOC spectra with the literature. Even though much of the existing literature is based on measurements acquired with Green laser (~532 nm laser) Raman, which may produce spectral parameters such as relative peak intensities that are different from using a DUV excitation source, the Green laser Raman literature is more comprehensive than DUV laser Raman at this

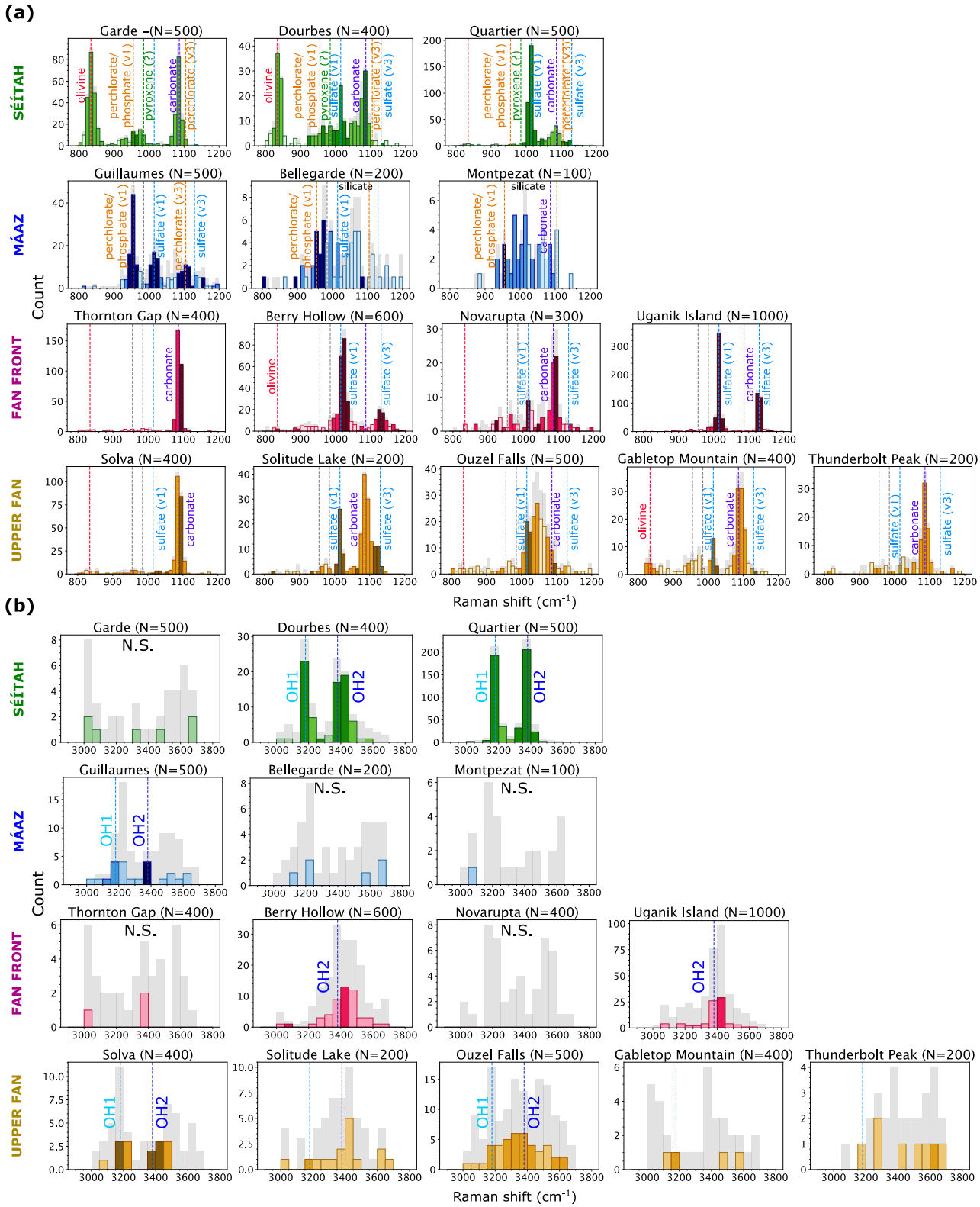

Figure 4.

time. Furthermore, for mineral and hydration peaks that are relevant in this work, while relative intensities change, the peak position is the same between DUV and Green laser Raman (e.g., Buzgar & Apopei, 2009; Prieto-Taboada et al., 2014; Razzell Hollis et al., 2021). When available, measurements done with the SHERLOC analog instruments Brassboard (Razzell Hollis et al., 2021) and ACRONM (Corpolongo et al., 2023), and the SHERLOC prototype instrument MOBIUS (Siljeström et al., 2024), which all use 248.6 nm DUV pulsed laser excitation source similar to SHERLOC, were also included in the literature compilation. Data from the SHERLOC Brassboard, ACRONM, and MOBIUS are labeled as so in the relevant figures where they are presented.

Due to the low spectral resolution of SHERLOC relative to lab data, the low SNR of the SHERLOC Raman spectra, and the limited detectability of signals at <800 cm^{-1} (Section 2.2), the detection of less intense peaks that can be diagnostic of a mineral species is often challenging. For a peak with SNR = 2, which is the lower threshold of peak detection in this work, the uncertainty of the fitted peak position is ~±8 cm^{-1} (Section 2.4). This uncertainty range covers the ν_1 peak position ranges of some mineral groups such as Ca-, Mg-, Fe-, Mn-carbonates (e.g., Buzgar & Apopei, 2009; Rividi et al., 2010) and Ca-, Mg-, Fe-sulfates of various hydration states (e.g., Chio et al., 2005; Prieto-Taboada et al., 2014; Wang et al., 2006). The accurate identification of a mineral species is also dependent on the availability of laboratory data, which may not be complete particularly for hydrated Mg-sulfates that have been previously identified at Jezero crater and Gale crater (Chipera et al., 2023; Siljeström et al., 2024). This is because the hydration states, structures, and crystallinity of hydrated Mg sulfates vary strongly and over wide ranges of water content depending on temperature and humidity conditions, not all of which have been studied in terrestrial labs at conditions relevant to Mars (see Section 4.3 and 4.4). Therefore, in this work, we have largely focused our identification of minerals to mineral groups rather than specific mineral species. However, when possible, specific species are identified in the data or recognized as being precluded by the data.

2.7. Comparison of SHERLOC Hydration Detections to SuperCam

SuperCam is a multi-technique remote-sensing instrument mounted on the rover's mast containing a 110 mm diameter telescope (Maurice et al., 2021; Wiens et al., 2021). SuperCam's typical mode of operation is to scan across a raster of observation points in linear (1 × 5, 1 × 10) or grid (3 × 3) patterns. For analyses of bedrock targets, SuperCam generally performs laser-induced breakdown spectroscopy (LIBS) first, as the shock waves from the laser pulses remove dust from natural surfaces. Typically, 30 pulses are administered per raster point; spectra from the first five pulses, which sample mostly dust, are discarded and the spectra from the last 25 are averaged. After LIBS, SuperCam typically makes passive UV, visible and near-infrared reflectance observations.

To compare SHERLOC hydration to that measurable with SuperCam, we use data from the near-infrared spectrometer (Fouchet et al., 2022), specifically calculation of the depth of the 1.9-μm H_2O combination bend and stretch absorption, which lies near the center of the spectrometer's range (1.3–2.6 μm). Other details of the infrared spectra of the Shenandoah formation and upper fan unit are covered elsewhere (e.g., Dehouck et al., 2023; Mandon et al., 2024). The field of view is 1.15 milliradians, amounting to several millimeters at the nominal abrasion patch distances of a little over 2 m. The spectra were calibrated to relative reflectance using pre-flight measurements and observations of a white target (AluWhite; Manrique et al., 2020) on the back of the rover. An empirical correction was also applied as a means to remove most of the atmospheric-related absorption bands (Royer, Fouchet, et al., 2023). We also use a hydration index derived from the H-alpha Balmer emission line at 656 nm in SuperCam's LIBS spectra. As LIBS does not easily quantify H abundances (e.g., Rapin et al., 2017), we use the ratio of the area under this peak divided by that under the oxygen triplet peak at 777 nm to provide a qualitative assessment of hydration via LIBS within the ~170–250 μm raster spots (Maurice et al., 2021) interrogated by the laser. The LIBS data were first pre-processed to provide wavelength calibration and to remove non-laser-induced background and electron-induced continuum to produce Clean Data Record (CDR) spectra.

Figure 4. Histogram plots of peaks detected in each abraded target (Séítah = green, Máaz = blue, fan front (Shenandoah) = pink, upper fan = brown) at Raman shift positions for (a) the mineral region (peak positions 800–1,200 cm^{-1}) with bin size = 10 cm^{-1}, and (b) hydration region (peak positions 3,000–3,700 cm^{-1}) with bin size = 50 cm^{-1}. Gray bars represent average SNR > 1, light-colored bars represent peaks of 2 < average SNR ≤ 3, medium-colored bars represent peaks of 3 < average SNR ≤ 5, dark-colored bars represent peaks of average SNR > 5. Vertical dashed lines indicate peak positions of mineral or hydration detections. Vertical lines are labeled only when detections are SNR > 3. In (a), silicate is labeled horizontally at ~1,000 cm^{-1} due to the variability of broad silicate peaks. Gray vertical lines at 955 and 985 cm^{-1} indicate possible artifacts which are currently investigated by the SHERLOC team and not discussed in this work.

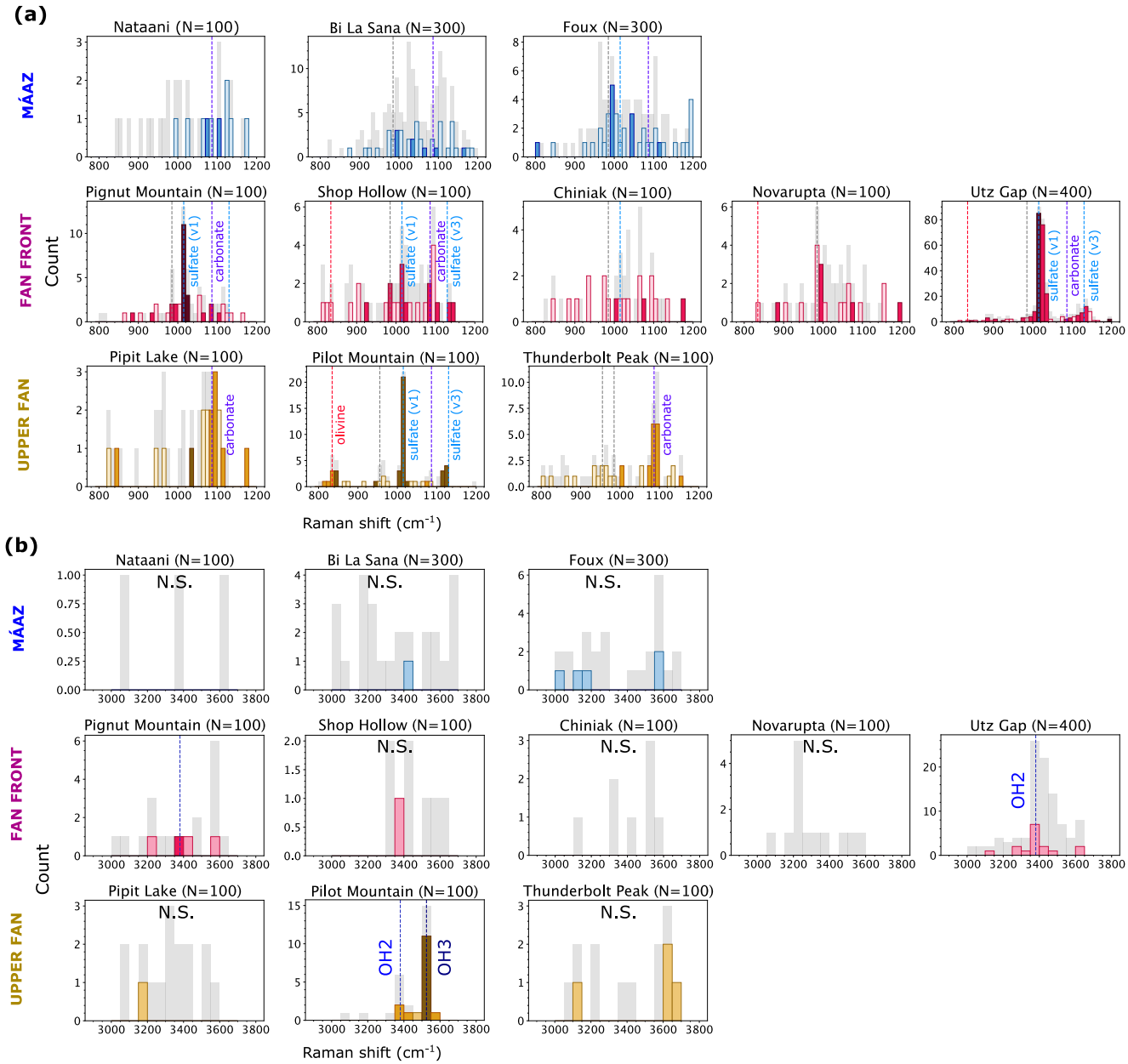

Figure 5. Histogram plots of peaks detected in each natural surface target (Máaz = blue, fan front (Shenandoah) = pink, upper fan = brown) at Raman shift positions for (a) the mineral region (peak positions 800–1,200 cm^{-1}) with bin size = 10 cm^{-1}, and (b) hydration region (peak positions 3,000–3,700 cm^{-1}) with bin size = 50 cm^{-1}. Gray bars represent average SNR > 1, light-colored bars represent peaks of 2 < average SNR ≤ 3, medium-colored bars represent peaks of 3 < average SNR ≤ 5, dark-colored bars represent peaks of average SNR > 5. Vertical dashed lines indicate peak positions of mineral or hydration detections. Vertical lines are only labeled when detections are SNR > 3. In (a), gray vertical lines at 955 and 985 cm^{-1} indicate possible artifacts which are currently investigated by the SHERLOC team and not discussed in this work.

3. Results

3.1. Phases Identified

In Figure 3, we present representative spectra of each phase detected, as described below. Each spectrum in Figure 3 has been processed using the methods described in Section 2, with fitted peak positions indicated by vertical dashed lines. The identification of phases was done by comparing the fitted peak positions of SHERLOC spectra with the literature and/or Brassboard/MOBIUS/ACRONM measurements, as described in Section 2.6.

We identified peaks of primary phase olivine and pyroxene mostly in the crater floor Séítah formation (Figure 3a). Broad peaks with variable shapes and peak positions that range from 960 to 1,110 cm^{-1} are assigned as silicate, following Corpolongo et al. (2023). It is challenging to assign the broad silicate peaks to a specific silicate phase because the prominent Raman peaks that can be used for phase identification such as feldspars are found at <800 cm^{-1}, below the effective Raman spectral region on SHERLOC (Section 2.2).

The alteration phases detected by SHERLOC include perchlorate and/or phosphate, sulfates, and carbonates (Figure 3a). The main peak corresponding to the ν_1 symmetric stretch mode of both perchlorate and phosphate is commonly found at ~950 cm^{-1}, so it is not possible to definitively distinguish between perchlorate and phosphate without secondary peaks (Corpolongo et al., 2023; Razzell Hollis et al., 2021; Scheller et al., 2022). The ν_1 symmetric stretch mode of sulfates is observed at ~1,000 cm^{-1}, while the ν_3 asymmetric stretch mode of sulfates at ~1,100 cm^{-1} is only sometimes observed, for example, in "Sol 618 Uganik Island Detail 1 point 18" but not in "Sol 304 Quartier Detail 3 point 77" (Figure 3a). The ν_1 symmetric stretch mode of carbonates is observed at ~1,080 cm^{-1}. However, the peak positions, peak widths and—specific to sulfates—the absence/presence of secondary peaks are variable between targets, which could imply differences in the specific sulfate and carbonate phases between targets, for example, solid solution variation in cation composition, or mixing of phases.

Hydration peaks are detected across both the crater floor and the western fan (Figure 3b). All hydrated spectra shown in Figure 3b have associated sulfate peaks in the mineral region. For some hydrated targets particularly in the crater floor, a perchlorate and/or phosphate peak is detected in addition to sulfate peaks, such as in the spectrum of "Sol 162 Guillaumes HDR 1 point 1" (Figure 3b). There are four characteristic expressions of hydration in SHERLOC Raman spectra (Figure 3b):

1. a bimodal spectral feature with peaks at ~3,200 and ~3,400 cm^{-1} as seen in Dourbes, Quartier, and Guillaumes in the crater floor, and Solva and Ouzel Falls in the upper fan. The ratio of intensity of the ~3,200 cm^{-1} peak to ~3,400 cm^{-1} peak (OH1 peak:OH2 peak; as labeled in Figure 3b) varies depending on target;
2. an asymmetric feature that contains more than one Gaussian component but only a single peak at ~3,400 cm^{-1} as seen in the fan front target Berry Hollow;
3. a unimodal Gaussian feature with a single peak at ~3,400 cm^{-1} as seen in the fan front target Uganik Island;
4. narrow feature with a more intense, lower wavenumber hydration peak at ~3,550 cm^{-1} and the higher wavenumber peak not as clearly resolved, as seen in the natural surface target Pilot Mountain in the upper fan.

To identify distinctive trends in alteration and hydrated phases across units, occurrences of peaks in all scans obtained from the same targets were stacked into histograms, according to thresholds described in Section 2.5 (Figure 4 for the abraded targets and Figure 5 for the natural surface targets). The bin size in the mineral region was set at 10 cm^{-1}, which is approximately the maximum peak position uncertainty. The bin size in the hydration region was set arbitrarily at 50 cm^{-1}. The overall trends observed in assigned/non-assigned minerals/hydration were consistent at other smaller or larger bin sizes such as 5 or 20 cm^{-1} for the mineral region, and 30 or 100 cm^{-1} for the hydration region.

SHERLOC single point data can be noisy, and work is ongoing to optimize processing. SNR > 1 peaks are shown in light gray. Colored bars are detections above our SNR > 2 threshold; darker color hues indicate greater SNRs, for example, >3 or >5. In general, higher SNRs as well as more occurrences of a peak at a given wavenumber provide greater confidence mineral detections. For some targets, there were only 1 or 2 spectra out of ≥100 with peaks at $2 < SNR \leq 3$ (a 0.3%–5% probability that these peaks are false positives) and no higher SNR peaks. These have been labeled "N.S." indicating no significant peaks are present and are treated as non-hydrated in this work. The vertical lines in Figures 4 and 5 indicate peak positions of minerals or hydration. When the detection is $2 < SNR \leq 3$, the vertical lines are not labeled with the phases as the SNR is too low to confidently assign a mineral identification to these peaks. Future, more robust data processing methods may allow more refined analysis of these spectra.

All but two targets (Nataani and Pipit Lake) show detections at 955 and/or 985 cm^{-1}, where peaks of perchlorate, phosphate, and pyroxene are commonly found, as previously described for the crater floor (Corpolongo et al., 2023; Scheller et al., 2022). Perchlorate and/or phosphate detections in the crater floor abraded targets are SNR > 5, but peaks in the fan front and the upper fan are typically at lower SNR. At the time of this writing, these weak, variable-position peaks are under investigation as potential measurement artifacts and, consequently, are not treated as mineral detections.

3.2. Mineral Detections by Formation

3.2.1. Crater Floor Séítah Formation

The Séítah formation of the crater floor is the stratigraphically oldest unit in Jezero crater that has been explored by the Mars 2020 rover (Farley et al., 2022; Stack et al., 2024). Orbital spectroscopic signatures of the Séítah formation are dominated by olivine, with limited detections of hydration and carbonation (e.g., Ehlmann et al., 2008, 2009; Goudge et al., 2015; Horgan et al., 2020). In situ investigations by the Mars 2020 rover confirmed the igneous nature of Séítah rocks, which have millimeter-size olivine grains in a matrix mainly composed of clinopyroxene. Evidence of aqueous alteration was also observed in Séítah rocks, including rims of carbonate around olivine grains, as well as millimeter to submillimeter-size bright patches of sulfate salts. However, the low proportions of these alteration phases suggest limited alteration (Farley et al., 2022; Horgan et al., 2020; Liu et al., 2022; Wiens et al., 2022).

The phases identified in Séítah in Figure 4 are largely consistent with previous analyses of SHERLOC Raman spectra (Corpolongo et al., 2023; Scheller et al., 2022; Siljeström et al., 2024). The agreement of our results with previous works validates the data analysis procedure as well as the use of a histogram statistical approach to phase identification, which contrasts with the point-by-point analyses done in previous works. Both primary and alteration phases are detected in Séítah (Figure 4). The detections of olivine and pyroxene in Garde and Dourbes are consistent with Corpolongo et al. (2023). The peaks identified as pyroxene in Quartier in Figure 4a were not previously identified in Corpolongo et al. (2023). Consistent with previous studies, perchlorates, and/or phosphates and carbonates are observed in all three abraded targets in Séítah whereas sulfates are detected only in Dourbes and Quartier (Corpolongo et al., 2023; Scheller et al., 2022; Siljeström et al., 2024).

Dourbes and Quartier show bimodal peak distributions in the hydration region, which is consistent with the bimodal hydration peaks in their spectra (Figure 3b). By contrast, Garde shows neither sulfate detections nor hydration peaks. This mineralogical correlation potentially signals that sulfates are the hydration carrier phases, as reported in Siljeström et al. (2024). The ratio of sulfate-to-carbonate detections is approximately 0.8 in Dourbes. In Quartier, this ratio is 0.7, when considering only the HDR scan, which captured both a white patch that was identified as sulfates and its surrounding materials, and not the four detail scans, which intentionally targeted the white patch.

3.2.2. Crater Floor Máaz Formation

The Máaz formation of the crater floor overlies and is interpreted to be younger than the Séítah formation (Farley et al., 2022). The Máaz formation is characterized from orbit to be olivine and pyroxene-dominated, with limited detections of hydration (e.g., Ehlmann et al., 2008; Goudge et al., 2015; Horgan et al., 2020). In situ investigations by the Mars 2020 rover confirmed the igneous nature of Máaz rocks which have submillimeter to millimeter-size pyroxene and plagioclase grains. Máaz also showed evidence of limited aqueous alterations with porosity-filling millimeter-size white patches of mixtures of sulfate and perchlorate salts and igneous grains with patches containing phyllosilicates and oxyhydroxides (Farley et al., 2022; Mandon et al., 2023; Scheller et al., 2022).

Our analyses of SHERLOC Raman spectra show that perchlorate and/or phosphate are observed in all abraded targets in Máaz (Figure 4). Sulfates are observed in Guillaumes and Bellegarde, and carbonates in Montpezat, as observed in previous works (Corpolongo et al., 2023; Scheller et al., 2022; Siljeström et al., 2024). Some peaks in Montpezat are consistent with broad silicate peaks with variable peaks positions in the range of 960–1,100 cm^{-1} (Figure 3a).

Only the Guillaumes target shows hydration detections. The bimodal hydration features in Guillaumes are similar to the hydration peaks observed in the Séítah rocks (Figures 3b and 4b). The hydrated phases in Guillaumes are detected within or close to the boundaries of white materials that are identified as sulfates and sometimes have concurrent detections of perchlorate and/or phosphate peaks (Corpolongo et al., 2023; Siljeström et al., 2024; Figure 3b). Bellegarde, which also has sulfate detections, does not have hydration detections, consistent with Siljeström et al. (2024).

The proportion of total scan points of all targets in Máaz showing hydration detections is 1%, less than that of Séítah (5%), even after excluding the four detail scans in Séítah's Quartier that intentionally targeted a white patch

that was identified as sulfates. However, the SHERLOC measurement areas are relatively small (up to 7 × 7 mm for HDR scans). This may add to some uncertainties with regards the contributions of sampling bias to the mineralogical and hydration detections made here, especially considering the heterogeneous nature of the abrasion patches as observed by the Autofocus Context Imager (ACI) and WATSON images (Figure 2; Corpolongo et al., 2023; Scheller et al., 2022; Wogsland et al., 2023).

Nataani, Bi La Sana, and Foux were unabraded, natural surfaces and the first few targets for which SHERLOC scans were acquired. The low 100–300 ppp and low laser current of 20 A (laser current of 25 A were used at all other targets analyzed in this work) used at these targets (Table 1), coupled with the higher topography and dust cover of natural surfaces give rise to higher noise levels that present challenges in mineral identifications. Even though there are a few counts of $2 < \text{SNR} \leq 3$ detections in the mineral region in all three of these natural surface targets, no minerals are assigned due to the low occurrences and low SNR of these detections.

3.2.3. Western Fan Front Shenandoah Formation

The sedimentary western Jezero fan is interpreted to have been emplaced after and overlies the igneous Séítah and Máaz formations of the crater floor (Stack et al., 2024). The lower ∼25 m of sedimentary rocks of the present-day Jezero western fan, which the Mars 2020 rover explored after exploring the crater floor, is referred to as the fan front and is informally named the Shenandoah formation (Stack et al., 2024). The stratigraphically higher and younger unit above the fan front is the upper fan named the Tenby formation (e.g., Siebach et al., 2023; Section 3.2.4).

From orbit, signatures of Fe/Mg-smectite clays and carbonates are found widely distributed across the fan front (Ehlmann et al., 2009; Goudge et al., 2017; Horgan et al., 2020). These alteration minerals suggest that the western fan is composed of materials that experienced aqueous alteration by fluid with near-neutral pH in the source region and/or depositional environment. Image observations from the WATSON and ACI cameras on the rover indicate that the Shenandoah formation is a sedimentary unit dominated by sandstone, with siltstone grain sizes observed only in the abraded target Uganik Island (Benison et al., 2024; Stack et al., 2024; Figure 2).

The SHERLOC mineral detections in the fan front targets are dominated by alteration phases with only Berry Hollow showing two instances of olivine detections (Figures 4a and 5a). Unlike the crater floor Séítah and Máaz formations where multiple alteration phases commonly co-occur in the same target, there is less mineralogical diversity of alteration phases within targets in the fan front. Most targets are dominated by sulfates (Berry Hollow, Uganik Island, Pignut Mountain, Utz Gap), and one target is dominated by carbonates (Thornton Gap).

Only one abraded target in the fan front, Novarupta, shows greater than 10 occurrences of both carbonate and sulfate detections. The ratio of sulfate-to-carbonate detections in Novarupta is 0.4, approximately two times smaller than the co-occurring sulfate and carbonate targets Dourbes and Quartier in Séítah. Hydration and perchlorate and/or phosphate phases are not detected in Novarupta, unlike Dourbes and Quartier. Thus, while Novarupta contains co-occurring sulfate and carbonate like the crater floor targets, it still exhibits differences in mineralogy of the alteration phases from the crater floor targets.

The natural surface scan of the abraded target Novarupta did not show any mineral phase detections. This is likely related to the presence of Fe^{3+}-bearing dust and higher topography of natural surfaces; the SHERLOC spectrometer is unable to focus at each point within a map on a target with high topographic relief. The natural surface target Shop Hollow shows detections of both sulfates and carbonates but with fewer than 10 detections each.

Hydration signatures are not observed in the carbonate-dominated target (Thornton Gap) but are found in sulfate-dominated abraded targets Berry Hollow and Uganik Island (Figure 4b). The natural surface target Pignut Mountain shows one hydration detection of $\text{SNR} > 3$ at 3,400 cm^{-1} (Figure 5b). Another natural surface target, Utz Gap, shows 14 counts of hydration detections but all of $\text{SNR} \leq 3$. The distribution of the $2 < \text{SNR} \leq 3$ detections falling within the $1 < \text{SNR} \leq 2$ detections suggests possible Utz Gap hydration. This was confirmed by analyzing the median spectra, which showed hydration detection.

Hydration is associated with sulfates, similar to what was observed in the crater floor. However, not all spectra that show sulfate detections are hydrated. There are almost 7 times as many sulfate detections as hydration detections in Uganik Island. In both Berry Hollow and Uganik Island, in addition to the primary sulfate peak

Table 2
ν_1 and ν_3 Sulfate and OH Stretch Mode Peak Positions in Wavenumber (cm^{-1}) for Anhydrite, Soluble Anhydrite, Bassanite, and Gypsum (Prieto-Taboada et al., 2014; Schmid et al., 2020; Wei et al., 2015)

	Anhydrite	Soluble anhydrite	Bassanite	Gypsum
ν_1	1,016.5–1,017.5	1,025–1,028	1,015–1,016	1,007.5–1,008.5
ν_3	1,111–1,112	1,145–1,149	Multiple peaks at 1,116–1,181	1,134–1,135
	1,128–1,129	1,152		
	1,159–1,160	1,167–1,172		
H_2O			3,553–3,554	3,401–3,407
			3,613–3,616	3,491–3,494

corresponding to the ν_1 symmetric stretch mode, secondary sulfate peaks corresponding to the ν_3 asymmetric stretch mode are observed. The variations in the Ca-sulfate Raman ν_1 and ν_3 peak positions found in the literature for a particular endmember phase (Table 2) can be due to differences in the spectral resolution of different instruments and/or variations in the sample such as sample purity and inherent strain in the crystal structure (Prieto-Taboada et al., 2014; Schmid et al., 2020). For example, the ν_3 subpeaks of anhydrite are less resolved in the spectrum measured with MOBIUS DUV laser than that measured with the 514.5 nm laser likely because of the different FWHM spectral resolutions of MOBIUS (25 cm^{-1}; Sapers et al., 2019) and the Renishaw Raman inVia Spectrometer (1,800 lines/mm grating used to give spectral resolution of 6 cm^{-1}) (Figure 6a).

The modes of the sulfate ν_1 and ν_3 peak positions observed in Berry Hollow and Uganik Island are more similar to anhydrite and bassanite than gypsum (Figures 4a and 6a), though the sulfate ν_3 peaks in Berry Hollow and Uganik Island are not resolved into three or more subpeaks as reported in some high spectral resolution literature data (Table 2). Nevertheless, the sulfate ν_3 peaks obtained with SHERLOC are similar in shape and have peak positions consistent with the spectrum of anhydrite measured with MOBIUS, which is a SHERLOC prototype instrument with a similar spectral resolution to SHERLOC. The non-hydrated sulfates in Berry Hollow and Uganik Island are thus likely to be anhydrite. Even though anhydrite is a nominally anhydrous phase, hydration peaks with peak positions and shapes that do not match gypsum or bassanite are sometimes found in SHERLOC spectra with sulfate peaks that closely match anhydrite (Figure 6a). Because no other mineral peaks are observed, it is possible that the hydrated phase in these anhydrite-dominated spectra is also a sulfate (see further discussion in Section 4.3).

The hydration features in the fan front members show only one peak at ~3,400 cm^{-1}, which is different than the bimodal hydration peaks at ~3,200 and 3,400 cm^{-1} in the crater floor formations (Figure 3b). Also, the modes of the OH2 hydration peaks (at ~3,400 cm^{-1}; as labeled in Figure 3b) are upshifted by 50 cm^{-1} (one bin) relative to the crater floor. These differences suggest that even though the hydration carrier phase is likely sulfates in both the crater floor and the fan front, the cation chemistry and/or hydration states of the sulfates are possibly different between the two units.

3.2.4. Western Upper Fan

The Shenandoah fan front transitions into the Tenby formation of the upper fan over a general area rather than a sharp contact (Siebach et al., 2023). From orbit, Fe/Mg-smectite and Mg-carbonate signatures are detected in the upper fan (Ehlmann et al., 2009). From ACI and WATSON images, the upper fan targets appear coarser-grained than the Shenandoah formation (Figure 2). The lower sections of the upper fan, which are mapped from orbit as the curvilinear unit (Stack et al., 2020), are primarily made up of sandstones. The grain sizes increase up the stratigraphy to conglomerates near the top of the upper fan (Figure 2; Siebach et al., 2023).

Other than detections of olivine in Gabletop Mountain, all upper fan abraded targets exhibit similar mineral assemblages; both sulfate and carbonate are observed in all (Figure 4a). However, the secondary sulfate ν_3 peak, which at the fan front indicated the presence of Ca-sulfates, is not detected in Solva. The ratio of sulfate-to-carbonate detection is variable across targets: 0.04 in Solva (effectively a carbonate-dominated target), 0.5 in

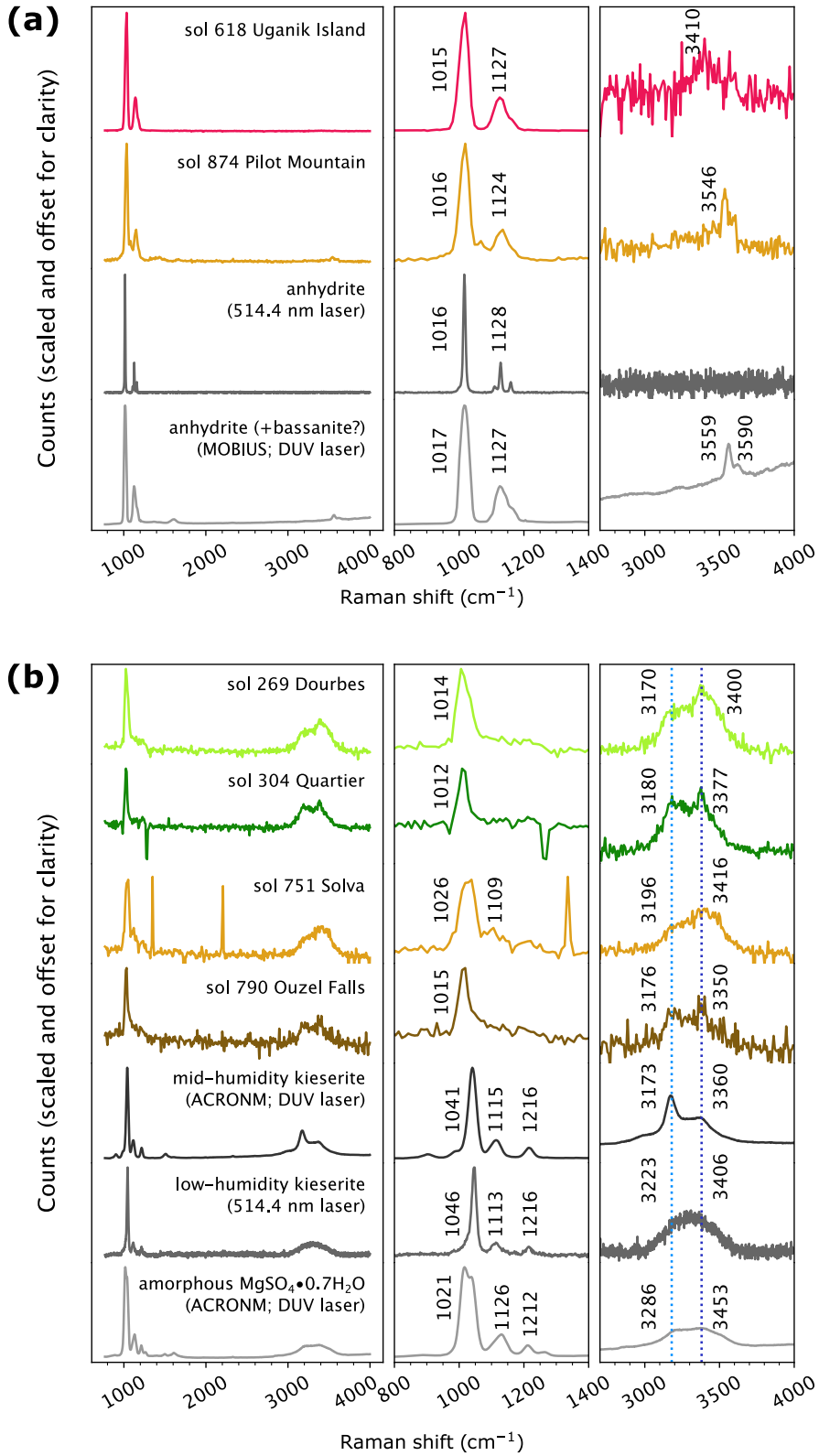

Figure 6.

Solitude Lake, 1.4 in Ouzel Falls, 0.3 in Gabletop Mountain, and 0.2 in Thunderbolt Peak. The ratio of sulfate-to-carbonate detection is smaller in both the fan front and upper fan targets compared to the crater floor Séítah targets, except Ouzel Falls, which is the only target across all four units that has more sulfate than carbonate detections. Ouzel Falls is also noteworthy in that the peak position distributions of both sulfate and carbonate are wider than other targets. In fact, from a statistical perspective, there is no clear separation between the sulfate and carbonate distributions in histograms (Figure 4a). It is unclear if the broad peak position distribution observed in Ouzel Falls is due to the broadness of the sulfate peak (Figure 3a) and/or a result of true solid solution variation in the phases leading to an upshifted sulfate peak (>1,020 cm^{-1}) and a downshifted carbonate peak (<1,070 cm^{-1}).

In contrast to the abraded targets which show co-occurrence of sulfates and carbonates in the same target, the natural surface targets only show single alteration phase identifications. Pipit Lake and Thunderbolt Peak show detections of carbonates with no hydration signatures. Pilot Mountain shows detections of olivine and sulfates. In Pilot Mountain, the peak positions of the primary ν_1 and secondary ν_3 sulfate peaks closely match Ca-sulfates (Figure 6a; Table 2). The mode of the ν_3 sulfate peaks in Pilot Mountain is upshifted by one bin (10 cm^{-1}) relative to other targets that have SNR > 5 secondary sulfate peak detections (Berry Hollow and Uganik Island in the fan front, and Solitude Lake in the upper fan; Figures 4a and 5a).

Hydration signatures are observed with high confidence in Solva and Ouzel Falls and, like other geologic units, are associated with sulfate peaks (Figures 3b and 4b). Solva shows bimodal distribution of the hydration peaks similar to the crater floor. While some hydrated spectra in Ouzel Falls also show bimodal peaks (e.g., Figure 3b), the broad distribution in Figure 4b suggests that the peak positions of OH1 and OH2 peaks (hydration peaks at ∼3,200 and ∼3,400 cm^{-1}, respectively; as labeled in Figure 3b) are more variable within Ouzel Falls than other targets showing bimodal hydration peaks. Solitude Lake yields 12 low-SNR hydration detections with most at ∼3,400 cm^{-1}. Gabletop Mountain and Thunderbolt Peak have few detections above our SNR threshold.

Pilot Mountain is the only natural surface target analyzed in this work that shows SNR > 5 hydration detections. The mode of the hydration peaks observed in Pilot Mountain is upshifted by three bins (150 cm^{-1}) relative to the crater floor, and two bins (100 cm^{-1}) relative to the fan front hydrated targets. The hydration peak is also narrower than all other hydrated targets across all four units including the other upper fan hydrated targets (Figure 3b). An example of a hydrated spectrum at Pilot Mountain with annotated peak positions is shown in Figure 6a. The sulfate ν_1 and ν_3 peak positions are similar to the spectrum of Uganik Island, which we have identified as anhydrite based on the hydration peaks at Uganik Island being dissimilar in peak position and shape to bassanite or gypsum (Section 3.2.3; Table 2). However, the peak position for the hydration peak (3,546 cm^{-1}) in the spectrum of Pilot Mountain is relatively close to the hydration peak of bassanite reported in the literature (Table 2). In the literature, two OH stretch peaks are sometimes reported for bassanite (Schmid et al., 2020; Wei et al., 2015) while some studies only report a single peak at ∼3,550 cm^{-1} (Prieto-Taboada et al., 2014). Visual inspection of the spectrum in Figure 6a shows the possibility of a second peak at ∼3,600 cm^{-1} even though it was not fitted by the algorithm developed in this work. The ν_1 peaks are at similar peak positions for both anhydrite and bassanite while the ν_3 peaks are less consistently defined for bassanite than anhydrite (Table 2). Based on the sulfate ν_1 and ν_3 peak positions and the hydration peak positions and shape, it is likely that the Pilot Mountain spectrum shows bassanite, likely in mixture with anhydrite.

Figure 6. Colored SHERLOC spectra compared to grayscale lab reference spectra. The sulfate ν_1 and ν_3 peak positions and the hydration peak positions are labeled. (a) Spectra of Uganik Island (Detail 1 point 32) and Pilot Mountain (point 31), compared to anhydrite obtained in the lab. Anhydrite (514.4 nm laser) was measured in this work (commercially available $CaSO_4$ from Sigma-Aldrich, >99%, Batch number MKCS6290, used without further characterization) with Renishaw Raman inVia Spectrometer using 514.4 nm excitation source. The spectrum of anhydrite measured on MOBIUS with a DUV laser is obtained from Siljeström et al. (2024), and contains minor amounts of hydration with peak positions that match those of bassanite (Prieto-Taboada et al., 2014; Wei et al., 2015; Table 2). (b) Spectra showing bimodal hydration peaks in Dourbes (Detail 1 point 28), Quartier (Detail 3 point 0), Solva (Detail 2 point 7), and Ouzel Falls (Detail 1 point 14), compared to kieserite of likely two structural polymorphs, mid-humidity and low-humidity (as defined in Wang et al. (2009), see Section 4.4 for more details), and amorphous $MgSO_4{\cdot}0.7H_2O$ spectra obtained in the lab. Spectrum of low-humidity kieserite was measured in this work (commercially available $MgSO_4{\cdot}H_2O$ from Sigma-Aldrich, >97%, Batch number BCCJ7021, used without further characterization) with Renishaw Raman inVia Spectrometer using 514.4 nm excitation source. Mid-humidity kieserite and amorphous $MgSO_4{\cdot}0.7H_2O$ spectra were measured on ACRONM with a DUV laser, and obtained from J. V. Clark et al. (2023) and Siljeström et al. (2024).

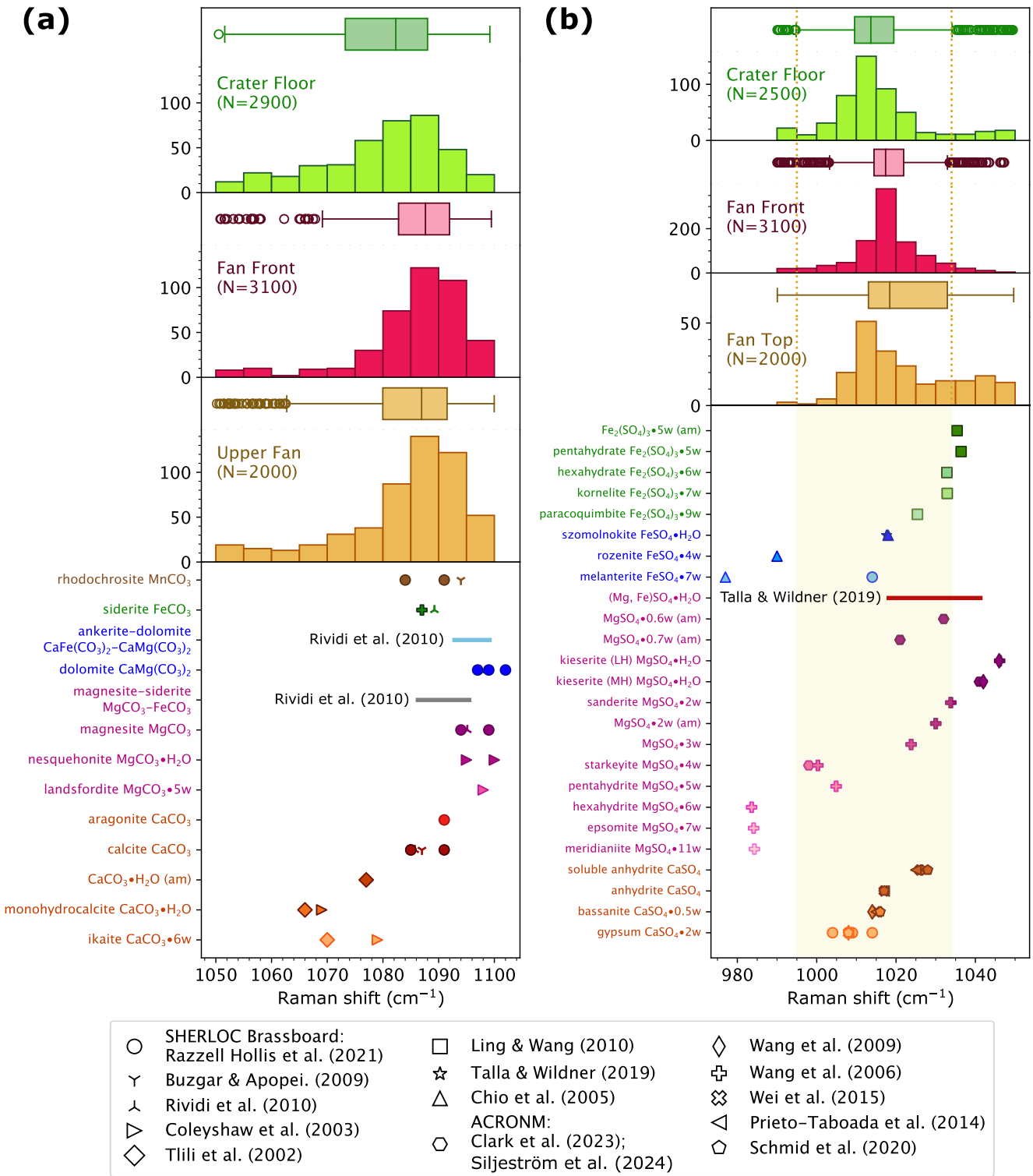

Figure 7.

3.3. Synthesis of Trends Across All Jezero Crater Units

3.3.1. Carbonate Mineralogy

The carbonate detections in each target as shown in Figures 4 and 5 have been further stacked by units in Figure 7a, with Séítah and Máaz grouped together as the crater floor, to examine trends in the carbonate Raman peak positions (defined by us as peaks in the range 1,050–1,100 cm^{-1}) across units. The proportion of carbonate detections out of the total scans is the highest in the upper fan at 27%, approximately two times the crater floor (14%) and the fan front (13%). The peak positions of the carbonate detections span the range of Ca/Mg/Fe/Mn. The medians of the carbonate peak positions are more similar in the fan front and upper fan units of the sedimentary western fan (1,087 cm^{-1}) and downshifted in the crater floor (1,082 cm^{-1}), possibly suggesting more Ca or Fe-rich compositions of the carbonates in the crater floor, and more Mg-rich compositions in the western fan. The observation of Fe-rich carbonates in the crater floor is supported by SuperCam (Clavé et al., 2023).

The carbonate peaks at lower wavenumbers are more prevalent in the crater floor and the upper fan with peak positions that are consistent with hydrous carbonates (Figure 7a). However, qualitative examination of individual spectra shows that carbonate peaks are not present in most spectra where hydration peaks are observed (Figure 3b). Some of these low-wavenumber peaks are shoulders on sulfate peaks (e.g., "sol 304 Quartier Detail 3 point 77" in Figure 3a). It is unclear if the asymmetry of some sulfate peak fits is caused by carbonates or a convolution of sulfates of varying hydration states such as anhydrous Mg-sulfate which has a peak at 1,052.7 cm^{-1} (Wang et al., 2006).

3.3.2. Sulfate Mineralogy

Similarly, the sulfate detections in each target as shown in Figures 4 and 5 have been further stacked by units in Figure 7b to examine the trends in the sulfate peak positions (defined by us as 990–1,050 cm^{-1}) across units. The proportion of sulfate detections out of the total scans is the highest in the fan front at 31%, followed by the crater floor (17%) and the upper fan (11%). These results indicate that the mineralogy of the fan front and the upper fan are distinct: the fan front is dominated by sulfates while the upper fan has almost two times more carbonate detections than sulfate detections. PIXL analyses of elemental composition report ∼20 wt.% SO_3 in the sulfate-dominated targets Berry Hollow and Uganik Island in the fan front, which is ∼25× greater than in the sulfate-containing crater floor target Dourbes (Liu et al., 2022; Stack et al., 2024). SuperCam observations also report the upper fan to be dominated by carbonates with no sulfate detections (Royer, Wiens, et al., 2023).

Similar to the carbonates, sulfate cations span the range of Ca/Mg/Fe across geologic units. There are some phases wholly inconsistent with the SHERLOC sulfate peak positions including highly hydrated Mg-sulfates (meridianiite, epsomite, hexahydrite) and most Fe(II)-sulfates (melanterite, rozenite). The median of the sulfate distributions of all three units are relatively similar: 1,014 cm^{-1} in the crater floor, 1,017 cm^{-1} in the fan front, 1,018 cm^{-1} in the upper fan. However, the range of sulfate peak positions is the broadest in the upper fan and the narrowest in the fan front, which is dominated by the large number of anhydrite detections (∼270 spectra) in Uganik Island. This implies that the sulfate mineralogy as detected with SHERLOC is more uniform across the targets in the fan front than in the upper fan. This contrasts with the carbonate mineralogy that is more similar between the fan front and the upper fan.

Figure 7. (top) Histogram plots of the peak positions of (a) carbonate and (b) sulfate detections in each unit, with Séítah and Máaz grouped together in the crater floor unit and bin size = 5 cm^{-1}. Peaks of SNR > 2 are included in this histogram. Boxplots showing the distribution of the peak positions are shown above each histogram. The left and right edge of the box represent the first and third quartiles, with the line in the box representing the median. The whiskers represent the minimum and maximum range of the data, defined to be within (the first quartile – 1.5 times the interquartile range) and (the third quartile + 1.5 times the interquartile range). The open circles represent values outside of the minimum and maximum range of the data. (Bottom) Peak positions of various hydrous and non-hydrous (a) Mn/Fe/Mg/Ca carbonate and (b) Fe/Mg/Ca sulfate phases from the literature with the ideal chemistry labeled along with their mineral names. The symbols represent the references that these peak position values were obtained from (Green laser Raman: Buzgar & Apopei, 2009; Chio et al., 2005; Coleyshaw et al., 2003; Ling & Wang, 2010; Prieto-Taboada et al., 2014; Rividi et al., 2010; Schmid et al., 2020; Talla & Wildner, 2019; Tlili et al., 2002; Wang et al., 2006, 2009; Wei et al., 2015; DUV laser Raman with ACRONM: J. V. Clark et al., 2023; Siljeström et al., 2024; DUV laser Raman with SHERLOC Brassboard: Razzell Hollis et al., 2021). The shaded region in (b) indicates the range of the sulfate peak positions of the crater floor as reference. "(am)" indicates amorphous phase; "w" indicates water per formula unit; "MH" and "LH" indicate mid- and low-humidity polymorph of kieserite, respectively as in Figure 6.

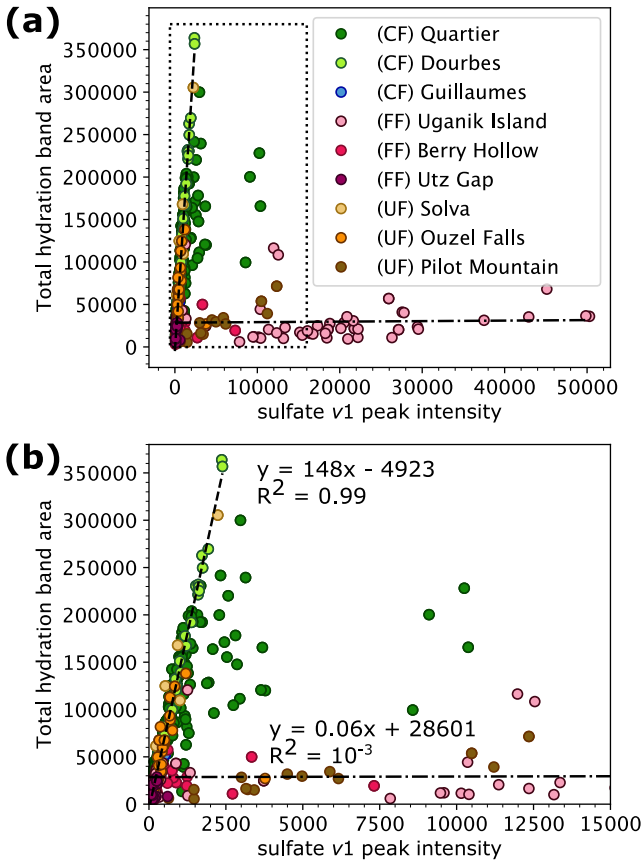

Figure 8. Total area of the hydration band at 2,800–3,900 cm^{-1} as a function of sulfate ν_1 peak intensity at ~1,000 cm^{-1} for the targets with observed hydration signatures, as defined in Figures 4 and 5. The range marked out in the rectangle in (a) is magnified in (b). The dashed line is a linear trendline fitted to points from Dourbes as was done in Siljeström et al. (2024) while the dash-dotted line is a linear trendline fitted to points from Uganik Island. CF = crater floor, FF = fan front, UF = upper fan.

3.3.3. Sulfate Hydration State and Cation

There are broadly three types of proportional relationships between the sulfate peak intensity and area of hydration band (Figure 8): (a) large increase in OH area with small increase in sulfate peak intensity as in Dourbes; (b) minimal increase in OH area with large increase in sulfate peak intensity as in Uganik Island; (c) spectra with behavior in between (a) and (b).

The crater floor targets and multiple fan targets (Utz Gap, some of Berry Hollow, and some of Uganik Island of the fan front; Solva and Ouzel Falls of the upper fan) exhibit relationship (a). This proportional increase of the hydration band area with the sulfate peak intensity supports sulfate, or a phase always co-occurring with sulfate, as the likely hydration carrier phase and one that is found within rocks across all units. Some of Berry Hollow and most of Uganik Island of the fan front follow relationship (b). Sulfate peaks that closely match anhydrite are observed in multiple points in these targets (Figures 4 and 6a), so the increasing sulfate peak intensity with a lack of corresponding increase of hydration suggests increasing anhydrite contribution to the spectra.

The spectral shapes of the hydration peaks are distinct between targets that follow relationship (a) and those that follow relationship (b). This implies that the differences in the degree of hydration are not only due to the differences in the proportion of contributions from anhydrite, but also due to differences in the compositions of the hydrated sulfates including hydration states and/or cations. Except for the small number of points from the fan front targets Berry Hollow, Uganik Island and Utz Gap, which have small hydration band areas, most points that follow relationship (a) have hydration peaks that are bimodal even though the ratio of intensity of OH1 peak:OH2 peak (~3,200 cm^{-1} peak:~3,400 cm^{-1} peak) is variable. By contrast, points that follow relationship (b) only have a single hydration peak visible in the spectra (Figure 3b; Section 3.1).

Pilot Mountain in the upper fan falls between relationships (a) and (b); it is more hydrated than the fan front points with anhydrite but much less hydrated than those that follow relationship (a). This is consistent with both the sulfate and the hydration peaks in Pilot Mountain closely matching those of bassanite (Figure 6a), which is more hydrated than the nominally anhydrous anhydrite, and increasing or decreasing proportions of bassanite in a SHERLOC spot may govern this trend. There are also a few tens of points from Quartier of the crater floor that plot between (a) and (b). However, the hydration peaks of these points are bimodal, similar to those that follow relationship (a), and do not match the hydration peaks of bassanite. These points in Quartier have some contributions of anhydrite that shift them off of relationship (a) toward relationship (b) (also observed by Siljeström et al. (2024)).

Figures 9a–9d show that hydrous sulfates measured in the lab have different, diagnostic combinations of sulfate ν_1 and hydration peak positions depending on the hydration states and/or cations. Hydrous Ca-sulfate is consistent with western fan spectra only, mostly in Pilot Mountain of the upper fan (cluster 3 in Figure 9e). A comparison of the combinations of the SHERLOC sulfate ν_1 peak position and the hydration peak position to literature values of lab measurements suggests that there are negligible detections of highly hydrated sulfates (consistent with Section 3.3.2) and that there are four types of hydrated sulfates with varying hydration state and/or cations:

1. One of two of the biggest clusters encompasses points from all three geologic units with sulfate ν_1 (~1,000–1,025 cm^{-1}) and hydration peak positions (~3,400 cm^{-1}) that are consistent with $MgSO_4{\cdot}nH_2O$ ($2 < n \leq 5$) (Figure 9a).
2. Another cluster has sulfate peak positions >1,025 cm^{-1} and hydration peak positions ~3,400 cm^{-1} and is comprised of a few points from the crater floor and more from the fan front and the upper fan. These peak

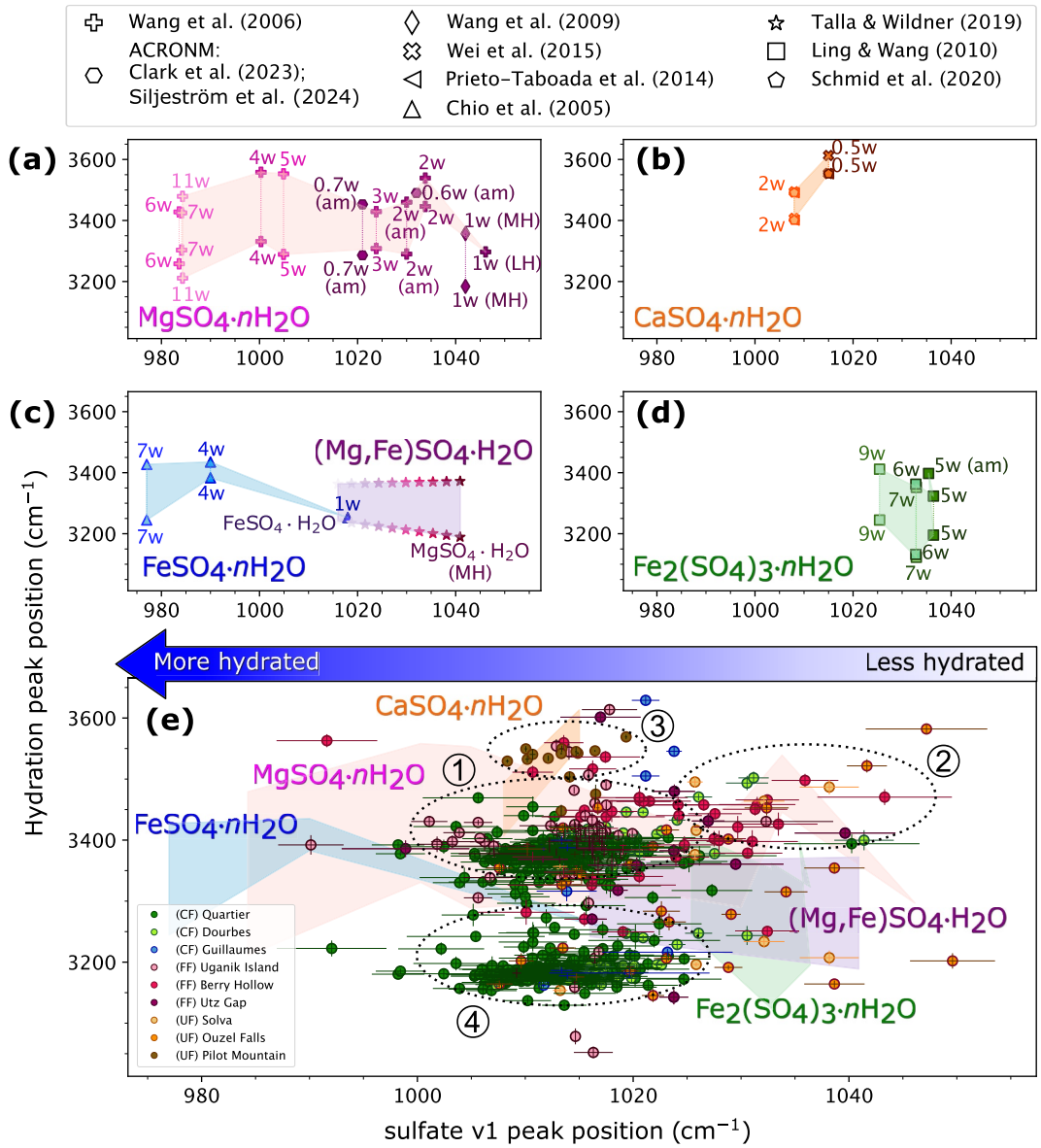

Figure 9. Hydration peak position as a function of sulfate ν_1 peak position for various hydrous sulfates measured in the lab: (a) $MgSO_4{\cdot}nH_2O$, (b) $CaSO_4{\cdot}nH_2O$, (c) $FeSO_4{\cdot}nH_2O$, and (Mg, Fe)$SO_4{\cdot}H_2O$, (d) $Fe_2(SO_4)_3{\cdot}nH_2O$ with values of n labeled in the plot. Hydration peak positions of one or two sub-peaks are shown in the plot. For compounds with hydration peaks of more than two sub-peaks, the minimum and maximum peak positions of the sub-peaks are plotted here. The area between the two sub-peak positions is shaded for clarity. The symbols represent the references that these peak position values were obtained from (Green laser Raman: Chio et al., 2005; Ling & Wang, 2010; Prieto-Taboada et al., 2014; Schmid et al., 2020; Talla & Wildner, 2019; Wang et al., 2006, 2009; Wei et al., 2015; DUV laser Raman with ACRONM: J. V. Clark et al., 2023; Siljeström et al., 2024). "(am)" indicates amorphous phase; "w" indicates water per formula unit; "MH" and "LH" indicate mid- and low-humidity polymorph of kieserite, respectively as in Figure 6. (e) Hydration peak positions as a function of sulfate ν_1 peak position as measured by SHERLOC. The circles are numbered according to the four hydrated sulfate spectral types described in the text. The shaded regions in (a)–(d) have been reproduced in (e). CF = crater floor, FF = fan front, UF = upper fan.

positions indicate Mg-sulfates of lower hydration states $MgSO_4{\cdot}nH_2O$ (n = 1–2) (Figure 9a). Siljeström et al. (2024) reported crystalline/amorphous Mg-sulfates of 3–5 waters, as well as possibly kieserite to be present in the crater floor. Our results here show that these Mg-sulfates of low hydration states are present across the fan front and the upper fan, as well.

3. A small cluster of points of fan spectra, including nearly all points of Pilot Mountain in the upper fan, have hydration peak positions >3,500 cm^{-1} and sulfate ν_1 peak positions consistent with hydrous Ca-sulfate. The band shapes in some of these spectra closely match bassanite (e.g., Figure 6a).
4. The other large cluster of points has sulfate peaks at ~1,000–1,025 cm^{-1} and hydration peaks at low wavenumbers of ~3,200 cm^{-1}. This combination of sulfate ν_1 and low wavenumber hydration peak positions does not significantly overlap with any known lab measurements of terrestrial sulfate samples.

4. Discussion

4.1. Summary of Observations as a Function of Geological Unit

A summary of the phases including hydration detections observed, arranged in the order of stratigraphic sequence, is given in Table 3. Olivine is observed in Séítah, in Pilot Mountain, and Gabletop Mountain close to the upper section of the upper fan, and in very minor amounts in Berry Hollow in the fan front. Sulfates and carbonates, separately or together, occur in targets across every geological unit, though the cations and/or hydration states of the sulfates and the cations of the carbonates vary across the units. The carbonates in the igneous crater floor appear to be more Fe-rich while those in the sedimentary western fan appear more Mg-rich (Figure 7a), consistent with SuperCam's observations of more Fe-rich composition in the crater floor (Clavé et al., 2023). It is, however, challenging to definitively constrain the Ca/Fe/Mg cation composition of the carbonates with SHERLOC Raman spectra, where only the carbonate peak corresponding to the ν_1 mode is observed.

Hydrated Mg-sulfates $MgSO_4{\cdot}nH_2O$ ($2 < n \leq 5$) are observed in both the crater floor and the western fan. Mg-sulfates of lower hydration degree ($n = 1$–2) become more prevalent in the western fan. Ca-sulfate is present as anhydrite in the floor and fan front that sometimes co-occurs with hydrated Mg-sulfate, but at stratigraphically higher reaches of the fan, the Ca-sulfate is bassanite.

Carbonate and sulfate co-occur in many targets in the crater floor and the upper fan. While the sulfates are detected in white materials that are rimmed by carbonates in both Dourbes and Quartier in the Séítah formation (Corpolongo et al., 2023; Siljeström et al., 2024), most sulfate and carbonate detections in the upper fan show no clear textural correlations except for some localized detections of sulfates in Solitude Lake and Ouzel Falls, where there are irregularly shaped, mm to sub-mm sulfate patches that appear to be pore-filling within the clastic grain matrix. In Dourbes, the carbonates are suggested to form as a result of olivine alteration, with sulfates later precipitating in areas that previously contained carbonates (Siljeström et al., 2024). The different textural correlations, lack of olivine detections, and more variable sulfate-to-carbonate detection ratios in the upper fan (Section 3.2.4) suggest distinct formation processes of the carbonates and sulfates in the fan than the crater floor (Section 4.7).

4.2. Non-Sulfate Hydrous Phases: Where Are the Hydrated Silicates?

Orbital spectroscopic observations show signatures of other non-sulfate hydrated phases such as Fe/Mg-smectite clays in the western fan (e.g., Ehlmann et al., 2008, 2009). The infrared spectrometer on the SuperCam payload on the Mars 2020 rover has also detected non-sulfate hydrated phases at the crater floor such as phyllosilicates and oxyhydroxides (e.g., Mandon et al., 2023), which have not been identified with SHERLOC in previous works. The thus far non-detection of phyllosilicates with SHERLOC is likely related to the low Raman scattering cross-sections of phyllosilicates (Wang et al., 2015).

We investigated possible contributions of phyllosilicates or other non-sulfate hydrated phases to the SHERLOC hydration spectra, using peak positions of phyllosilicates, zeolites, and hydrated silica, as compiled from the literature (Figure 10). Smectites measured under Earth-ambient have higher wavenumber peaks than those observed with SHERLOC, though future work should collect Raman spectra of collapsed smectites that mimic the low/no interlayer water state observed on Mars (Bristow et al., 2015, 2018). In addition to sulfates, opal-CT and monohydrocalcite have hydration peaks that are consistent with the SHERLOC data point cluster of low wavenumber hydration peaks at ~3,200 cm^{-1} that do not yet have a definitive identification (Figure 9e). However, both opal-CT and monohydrocalcite have mineral peaks at 1,060–1,090 cm^{-1} that are not observed in most SHERLOC spectra that show the hydration peaks at ~3,200 cm^{-1}, and thus are unlikely to be the hydration carrier phases as observed by SHERLOC than amorphous Mg-sulfate (see Section 4.4).

Table 3
Summary of Alteration Phases and Other Accompanying Phases in Each Target, Arranged in Stratigraphic Order From the Stratigraphically Highest at the Top

Unit/Lithology	Target name	Sulfate	Carbonate (by unit according to Figure 7a)	Other phases
Upper Fan (Tenby)				
fg Conglomerate	*Thunderbolt Peak*	–	*Mg-rich (+Fe): no textural correlation*	–
fg Conglomerate	Thunderbolt Peak	Anhydrous: no textural correlation	Mg-rich (+Fe): no textural correlation	–
fg Conglomerate	*Pilot Mountain*	*Hydrous Ca-sulfate (bassanite) of hydration type (4): bright sub-mm material*	–	*Olivine*
Sandstone	Gabletop Mountain	Anhydrous: no textural correlation	Mg-rich (+Fe): no textural correlation	Olivine
fg Conglomerate	Ouzel Falls	Mg 3–5w, Mg 1–2w Some bimodal hydration type (1): irregularly shaped mm filling pore	Mg-rich (+Fe): matrix	–
Sandstone	*Pipit Lake*	–	Mg-rich (+Fe): matrix	–
Sandstone	Solitude Lake	Anhydrite: irregularly shaped mm filling pore	Mg-rich (+Fe): matrix	–
Sandstone	Solva	Mg 3–5w, Mg 1–2w Bimodal hydration type (1): no textural correlation	Mg-rich (+Fe): widespread	–
Fan Front (Shenandoah)				
Sandstone	Uganik Island	Anhydrite: mm-sized white crystalline patch Mg 3–5w, Mg 1–2w Unimodal hydration type (3): tan interclast (Benison et al., 2024)	Mg-rich (+Fe) (minor amounts)	–
Sandstone	Thornton Gap	–	Mg-rich (+Fe): widespread	–
Sandstone	*Shop Hollow*	*Anhydrous (minor amounts)*	*Mg-rich (+Fe) (minor amounts)*	–
vf Sandstone	Berry Hollow	Anhydrite: sub-mm vein Mg 3–5w, Mg 1–2w Asymmetric Gaussian with one peak type (2) hydration: matrix	–	Olivine (minor amounts)
vf Sandstone	*Pignut Mountain*	*Anhydrous*	*Mg-rich (+Fe)*	–
vf Sandstone	Novarupta	Anhydrous	Mg-rich (+Fe)	
vf Sandstone	*Novarupta*	–	–	–
vf Sandstone	*Chiniak*	–	–	–
Sandstone	*Utz Gap*	*Mg 3–5w, Mg 1–2w*	*Mg-rich (+Fe) (minor amounts)*	–
Máaz				
Igneous rocks	*Nataani*	–	–	–
	Bi La Sana	–	–	–
	Guillaumes	Mg 3–5w Bimodal hydration type (1): white materials	–	Perchlorate and/or phosphate
	Foux	–	–	–
	Bellegarde	Anhydrous Ca-sulfate: white materials (Siljeström et al., 2024)	–	Perchlorate and/or phosphate Silicate
	Montpezat	–	Fe-rich (+Mg)	Perchlorate and/or phosphate Silicate

Table 3
Continued

Unit/Lithology	Target name	Sulfate	Carbonate (by unit according to Figure 7a)	Other phases
Séítah				
Igneous rocks	Quartier	Mg 3–5w (major)	Fe-rich (+Mg): rimming sulfate	Perchlorate and/or phosphate
		Mg 1–2w (minor)		
		Bimodal hydration type (1): white crystal		Pyroxene
		Anhydrite		
	Garde	–	Fe-rich (+Mg)	Olivine
				Perchlorate and/or phosphate
				Pyroxene
	Dourbes	Mg 3–5w (major)	Fe-rich (+Mg): rimming sulfate	Olivine
		Mg 1–2w (minor)		Perchlorate and/or phosphate
		Bimodal hydration type (1): white crystal		Pyroxene

Note. Natural surface targets are marked with italics. See Section 3.1 for description on hydration types. Textural features noted in this table are marked with arrows in Figure 2. fg = fine grained; vf = very fine in lithology description.

4.3. Hydrated Anhydrite?

In Uganik Island, hydration bands are sometimes observed in spectra with sulfate ν_1 and ν_3 peaks that closely match anhydrite (Figure 6a). The SuperCam IRS also showed hydration bands in some targets where anhydrite is observed (Lopez-Reyes et al., 2023). The peak shape and position (3,350–3,450 cm^{-1}; Figures 4b and 6a) of these hydration bands do not match that of hydrated Ca-sulfates gypsum or bassanite (Figure 6a; Table 2). Soluble anhydrite forms from the dehydration of gypsum or bassanite and has a crystal structure that is similar to bassanite except that the channels that accommodate water molecules in bassanite are empty in soluble anhydrite (Ballirano & Melis, 2009). While these empty channels in soluble anhydrite can adsorb water molecules and partially hydrate under certain thermodynamic conditions (e.g., up to 0.15 mol H_2O per mol $CaSO_4$ at ~120°C and H_2O partial pressure 60 hPa; Preturlan et al., 2019), the Raman spectra of soluble anhydrite do not show hydration peaks (Table 2; Prieto-Taboada et al., 2014; Schmid et al., 2020; Wei et al., 2015).

Ferric sulfates, ferrous sulfates, Mg-sulfates as well as some non-sulfate hydrated phases such as carbonates, smectites, and opal also have hydration peaks at 3,350–3,450 cm^{-1} (Figure 10). However, no peaks at 1,060–1,090 cm^{-1}, which would be expected for carbonates, are observed in these hydrated spectra in Uganik Island. Smectites commonly have hydration peaks at >3,500 cm^{-1} due to structural OH, which would be expressed as narrow peaks in contrast to the broad hydration bands due to molecular H_2O (Section 2.3). The hydrated spectra in Uganik Island do not show narrow peaks at >3,500 cm^{-1} (Figure 6a). Therefore, the hydration associated with spectra closely matching anhydrite is likely due to Fe/Mg-sulfates, whereby their sulfate ν_1 peaks are subsumed within the intense sulfate ν_1 peaks of anhydrite. This is similar to what Siljeström et al. (2024) had reported for Quartier in the crater floor Séítah formation, where they observed hydration bands to be present in spectra with anhydrite peaks, and suggested that these are due to the presence of some amounts of hydrated Mg-sulfates. Interestingly, the anhydrite-associated hydration bands observed in igneous rock at Quartier are bimodal while those in sedimentary rock at Uganik Island are unimodal (Figure 3b). Thus, the implication is that anhydrite occurs in mineral assemblages at <100 μm spatial scale with hydrated sulfates but that the associated hydrated sulfates are of different hydration states and/or cations in these two targets.

4.4. Identifying the Hydration State, Composition, and Crystallinity of Mg-Sulfates

Wang et al. (2006) showed that Mg-sulfates of different hydration states each have characteristic sulfate ν_1 peak positions as well as sub-peak structures in the hydration band, which can be used to identify the hydration states through Raman spectroscopy. The ν_3 asymmetric stretch mode of sulfates can provide further constraints on the

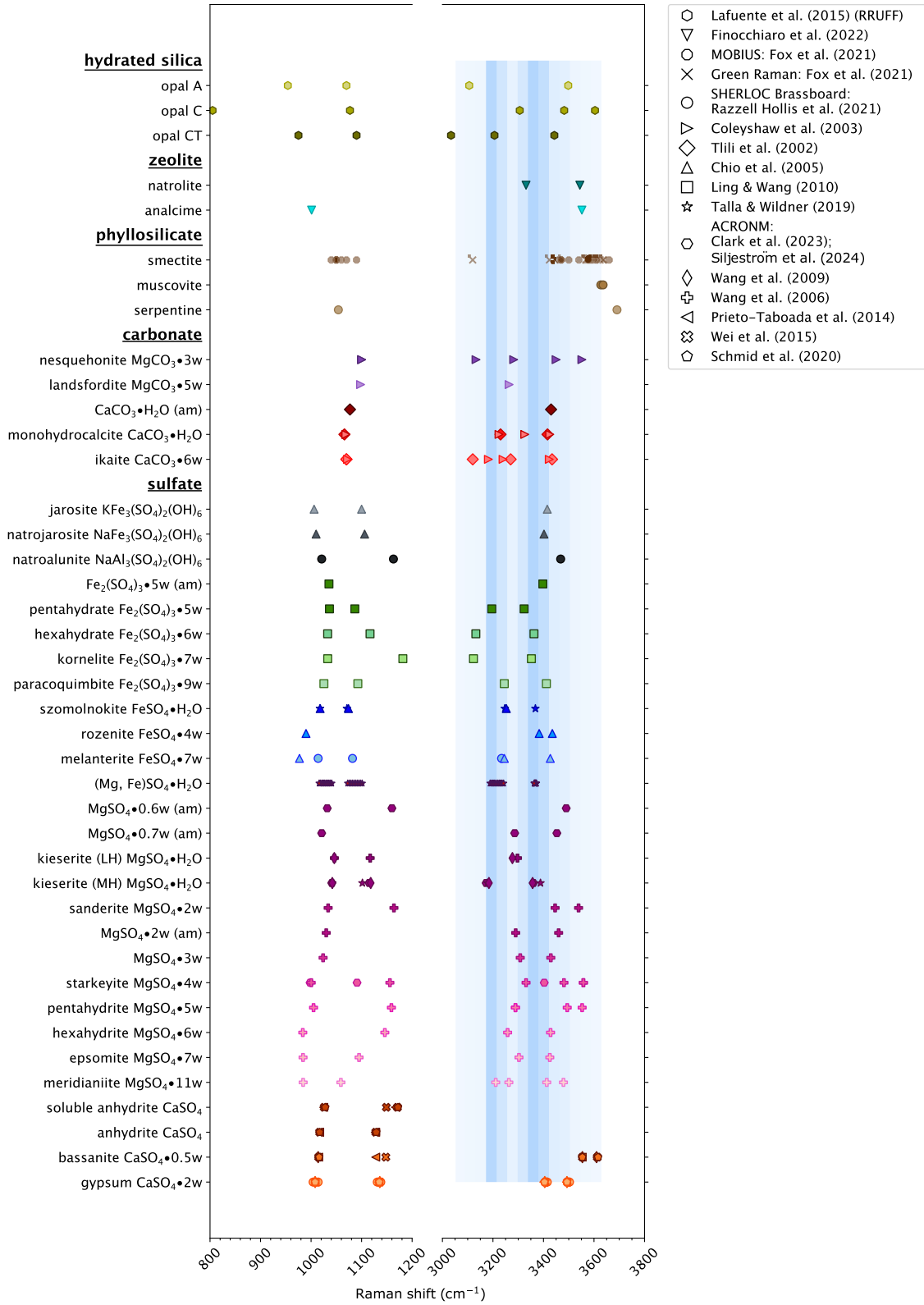

Figure 10.

hydration states of Mg-sulfates. However, the ν_3 asymmetric stretch modes are not well-resolved in SHERLOC Raman spectra, and the definitive identification of the hydration states of Mg-sulfates observed with SHERLOC based on comparison to library spectra has been challenging.

One reason for the difficulty of matching the hydration peak positions with library spectra is due to the variability in the fitted peak positions, which can have an uncertainty of $\sim\pm8$ cm^{-1} for a peak with SNR = 2 (see Section 2.4). This uncertainty range covers the sulfate ν_1 peak positions of $MgSO_4{\cdot}nH_2O$ (n = 3–5) (Wang et al., 2006). The sulfates can also be variable at small spatial scales within a SHERLOC laser spot in terms of cation composition and hydration due to changing conditions during fluid precipitation. That is, within the SHERLOC spot size there are likely multiple sulfate solid solutions and, perhaps, minerals or hydration states.

Another reason could be that the hydration states, structures, and crystallinity of hydrated Mg sulfates vary strongly and over wide ranges of water content depending on temperature and humidity conditions. In terrestrial labs, Wang et al. (2009) reported two polymorphs of kieserite: a low-humidity polymorph that is thermodynamically stable at less than 33% RH and a mid-humidity polymorph that is stable at higher than 33% RH. The two polymorphs of kieserite in Wang et al. (2009) have relatively similar sulfate ν_1 peak positions but show very different hydration features: a single broad hydration peak for the low-humidity kieserite and a bimodal hydration peak for the mid-humidity kieserite (kieserite spectra that closely match the low- and mid-humidity polymorph in Wang et al. (2009) are shown in Figure 6b). A low-temperature form of epsomite that has a distorted structure and is stable to ~13% RH at −10°C has also been reported. This low-temperature epsomite has similar sulfate ν_1 peak position to epsomite but very different hydration features (Wang et al., 2011). It is possible that, similarly, there are other phases of crystalline $MgSO_4{\cdot}nH_2O$ ($2 < n \leq 5$) with different atomic structures that are more favorable under the humidity and temperature conditions at Jezero crater but which have not been studied on Earth. This may be a remote possibility given the similar surface thermodynamic conditions at Jezero crater and Gale crater, at which only crystalline starkeyite and kieserite have been detected thus far with the X-ray diffraction instrument CheMin (Chipera et al., 2023; Tutolo et al., 2024). Nevertheless, if such unknown phases of crystalline $MgSO_4{\cdot}nH_2O$ ($2 < n \leq 5$) exist, we can expect these hydrated Mg-sulfates of different atomic structures to have hydration bands that are expressed differently than what have so far been studied in terrestrial labs.

In addition to crystalline phases, amorphous Mg-sulfates of various water content have also been synthesized in labs (Vaniman et al., 2004; Wang et al., 2006). Vaniman et al. (2004) suggested that at the very low humidity conditions of <1% RH recorded at the Mars surface, the amorphous phase rather than crystalline phase is the favored product of the dehydration of Mg-sulfates of high hydration states. Such X-ray amorphous sulfates have been detected by the CheMin X-ray diffraction instrument on the Curiosity rover at Gale Crater (Rampe et al., 2020; Smith et al., 2022). Siljeström et al. (2024) proposed amorphous $MgSO_4{\cdot}3H_2O$ to be present in the Jezero crater floor target Dourbes, based on the broadened primary ν_1 sulfate peak that has peak position consistent with crystalline $MgSO_4{\cdot}3H_2O$. Their results for the water content of amorphous Mg-sulfates are consistent with the Canaima target at Gale crater where the amorphous Mg-sulfate detected was calculated to have 3.2 water per formula unit (Chipera et al., 2023).

In this work, based on the combination of both the sulfate and hydration peaks, we suggest that amorphous $MgSO_4{\cdot}0.7H_2O$, which has ν_1 sulfate peak at 1,021 cm^{-1} and hydration peak at 3,286 cm^{-1} (J. V. Clark et al., 2023; Siljeström et al., 2024) plot close to the cluster of SHERLOC data points with hydration peaks at low wavenumber (~3,200 cm^{-1}; cluster 4 in Figure 9e). However, the hydration peak of this amorphous Mg-sulfate is still higher than the SHERLOC data points at ~3,200 cm^{-1} (Figures 6b and 9e) and does not present an exact match. The difficulty for definitively identifying the hydration state of Mg-sulfates with Raman spectroscopy is

Figure 10. The peak positions of the mineral peaks (800–1,200 cm^{-1}) and hydration peaks (3,000–3,800 cm^{-1}) of hydrated silica, zeolite, phyllosilicate, carbonate, and sulfate with the ideal chemistry for some minerals labeled along with their mineral names. The shaded region corresponds to the peak position range of SHERLOC hydration peaks, with darker colors indicating larger number of detections. The symbols represent the references that these peak position values were obtained from (Green laser Raman: Chio et al., 2005; Coleyshaw et al., 2003; Finocchiaro et al., 2022; Fox et al., 2021; Lafuente et al., 2015; Ling & Wang, 2010; Prieto-Taboada et al., 2014; Schmid et al., 2020; Talla & Wildner, 2019; Tlili et al., 2002; Wang et al., 2006, 2009; Wei et al., 2015; DUV laser Raman with ACRONM: J. V. Clark et al., 2023; Siljeström et al., 2024; DUV laser Raman with SHERLOC Brassboard: Razzell Hollis et al., 2021; DUV laser Raman with MOBIUS: Fox et al., 2021), "(am)" indicates amorphous phase; "w" indicates water per formula unit, "MH" and "LH" indicate mid- and low-humidity polymorph of kieserite, respectively as in Figure 6. Unlike Figure 9, all peak position values reported in the references are plotted here.

due to the limited availability of laboratory Raman spectral data, especially as the hydration content of amorphous Mg-sulfates does not necessarily take discrete integer values, is highly variable and difficult to constrain. A range of water contents of amorphous $MgSO_4{\cdot}nH_2O$ have been reported, from $n = 0.6$ to $n = 3$ (J. V. Clark et al., 2023; Siljeström et al., 2024; Vaniman & Chipera, 2006; Wang et al., 2009). The hydration bands of these amorphous phases are expressed differently over the continuous range of water contents, not all of which are necessarily known currently from terrestrial studies. For example, while Wang et al. (2009) reported that amorphous $MgSO_4{\cdot}3.1H_2O$ has a ν_1 sulfate peak at 1,021 cm^{-1}, similar to $MgSO_4{\cdot}0.7H_2O$ reported in J. V. Clark et al. (2023) and Siljeström et al. (2024), no results for the hydration peak were reported for $MgSO_4{\cdot}3.1H_2O$ in Wang et al. (2009). Therefore, recognizing the limits in the availability of lab data, in this work, we present amorphous $MgSO_4{\cdot}0.7H_2O$ as a possible phase without precluding the possibility that more hydrated amorphous Mg-sulfates such as that reported in Siljeström et al. (2024) for the crater floor and in Chipera et al. (2023) for the Canaima target at Gale crater are also present at the Jezero crater fan and floor.

These considerations of the role of humidity and the wide range of water content that Mg-sulfates can take have implications for samples returned to Earth and our ability to decipher fluid/climate conditions from the hydrated Mg-sulfates. These sulfates are unlikely to remain unchanged in the sealed returned samples because of differences in temperature and humidity relative to the Martian surface (Siljeström et al., 2024). Their manipulation on Earth may also be challenging because once the atmospheric gas head-space is extracted and the sample is exposed to a neutral (dry) atmosphere, the sulfates will dehydrate or, alternatively, rehydrate if they are exposed to the present-day environment of the Earth. The in situ SHERLOC data collected in the Mars environment motivate the need for further laboratory characterizations of both crystalline and amorphous phases of the hydrated sulfate systems at temperature and RH conditions relevant to the Mars surface to more definitively interpret the SHERLOC Raman spectra.

4.5. Hydration States of Mg-Sulfates at Multiple Landing Sites in the Present-Day Climate

The SHERLOC-detected sulfates have likely been exposed to large changes in temperature and RH since their formation. While sulfates have been identified at other landing sites, the Alpha Particle X-ray Spectrometer, Mössbauer Spectrometer and Miniature Thermal Emission Spectrometer (Mini-TES) on the Mars Exploration Rovers were not able to directly constrain the hydration states of the sulfates at Gusev crater and Meridiani Planum (Campbell et al., 2008; B. C. Clark et al., 2005). At Gale crater, changes in hydration states are observed during sample handling by the CheMin X-ray diffraction instrument on the Curiosity rover (Vaniman et al., 2004, 2018). The high spatial resolution of 100 μm/point and low sensitivity of the SHERLOC Raman spectrometer to other non-sulfate hydrated phases commonly found on Mars such as phyllosilicates (Wang et al., 2015) mean that the hydration signatures that SHERLOC directly detects can be more confidently assigned to sulfate phases than the hydration bands detected by the SuperCam IRS, which has a larger spot size and is sensitive to multiple hydrous phases. The SHERLOC Raman spectra of hydrated sulfates thus provide a unique opportunity to understand if these hydrated sulfates on Mars are in or out of equilibrium with present-day surface environmental conditions.

At Gale crater where the modern-day RH and temperature (0%–100% RH and ∼180 to ∼280 K; Chipera et al., 2023) are roughly similar to Jezero crater (Martínez et al., 2023; Polkko et al., 2023), starkeyite has been observed in two targets and kieserite in a different target with the CheMin instrument (Chipera et al., 2023; Tutolo et al., 2024). Our findings of two Mg-sulfate phases of different hydration states at Jezero crater are consistent with the CheMin analysis at Gale crater, with the high hydration phase $MgSO_4{\cdot}nH_2O$ ($2 < n \leq 5$) possibly consistent with starkeyite and the low hydration phase $MgSO_4{\cdot}nH_2O$ ($n = 1$–2) consistent with kieserite. However, it is curious that while both high and low hydration Mg-sulfates are found to sometimes co-occur in the same target at Jezero crater (Figure 9e; Siljeström et al., 2024), at Gale crater, crystalline Mg-sulfates of only one hydration state, either starkeyite or kieserite, is found in a single target. along with amorphous Mg-sulfate (Chipera et al., 2023; Tutolo et al., 2024).

We do not know why Mg-sulfates with multiple hydration states would be present in the same target in Jezero crater and not Gale crater, but we present three hypotheses. First, the sample processing carried out with CheMin, which measures drilled powder that is collected and analyzed within a warmer environment in the rover, is known to cause dehydration (Vaniman et al., 2018). This might cause the samples to be modified in ways that the in situ measurements conducted by SHERLOC do not. Another possibility is that there may be more variability at Jezero

crater than Gale crater in the absence/presence of other sulfates such as Ca-sulfates in physical contact with Mg-sulfates, which can influence Mg-sulfate hydration. For example, lab experiments showed pure epsomite dehydrated to starkeyite but when mixed with anhydrite, the dehydration product was kieserite (Wang et al., 2009). Such coexisting phases could have created localized RH conditions or act as catalysts to favor the dehydration to kieserite (Wang et al., 2009, 2011). This variation in the dehydration product of Mg-sulfates depending on the presence or absence of coexisting phases was proposed to explain the coexisting monohydrated and polyhydrated sulfate layers that have been observed from orbit on Mars such as at East Chondor Chasma (Wang et al., 2016). At Jezero crater, anhydrite and hydrated Mg-sulfates are sometimes present within the same SHERLOC spectra with a beam size of 100 μm (Figures 6a and 8, Siljeström et al., 2024). If anhydrite precipitated before or concurrently with the Mg-sulfate, then the Mg-sulfate in this mixed sulfate mixture may dehydrate to the low hydration phase $MgSO_4{\cdot}nH_2O$ (n = 1–2) while elsewhere within the same target where only Mg-sulfate is present, the dehydration product would be the high hydration phase $MgSO_4{\cdot}nH_2O$ ($2 < n \leq 5$). As CheMin measures drilled powder, the spatial relations between the different minerals detected in a sample are unclear. The Mg-sulfates and Ca-sulfates detected in the Canaima, Tapo Caparo and Ubajara drill samples could have been present at physically distinct locations before sampling, resulting in only either starkeyite or kieserite detected in each sample. A third possibility is that like Gale crater, only one of either the low or the high hydration phase at Jezero crater is crystalline while the other is amorphous. At the Canaima target at Gale crater, starkeyite was detected along with amorphous Mg-sulfate calculated to have 3.2 water per formula unit (Chipera et al., 2023). In this work, while we present amorphous $MgSO_4{\cdot}0.7H_2O$ as a possible amorphous Mg-sulfate phase present in Jezero crater, the limited laboratory data complicates efforts to definitively identifying the crystallinity of the Mg-sulfates based on Raman spectroscopy (Section 4.4).

In the following discussion, we will assume as most likely the scenario that the crystalline phases starkeyite and kieserite, which have both been detected at Gale crater (Chipera et al., 2023; Tutolo et al., 2024), are the high hydration phase $MgSO_4{\cdot}nH_2O$ ($2 < n \leq 5$) and the low hydration phase $MgSO_4{\cdot}nH_2O$ (n = 1–2) detected by SHERLOC at Jezero crater.

Measurements over one Martian year by Mars 2020's Mars Environmental Dynamics Analyzer (MEDA) instrument show that modern-day RH and temperature at Jezero crater span 0%–100% RH and 185–290 K on both diurnal and seasonal bases (Martínez et al., 2023; Polkko et al., 2023). Daytime relative humidities are close to 0, whereas maximum RH values are reached just prior to sunrise when the temperatures are minimal. In this temperature range, based on the phase diagram by Chipera et al. (2023), thermodynamics would dictate the dehydration/rehydration between epsomite, hexahydrite and starkeyite depending on humidity conditions. However, laboratory studies performed at −10°C and ∼80% RH showed that kieserite and starkeyite hydrate to epsomite after 288 hr while epsomite did not dehydrate over the duration of the experiment of ∼3.8 years (Wang et al., 2011). The present-day Mars temperatures are much lower than −10°C, implying that the kinetics will be much slower than the study by Wang et al. (2011). The dehydration and rehydration kinetics of hydrated Mg-sulfates are thus likely to occur over much longer timescales than the diurnal and seasonal cycles. This is corroborated by the findings of Siljeström et al. (2024), where they found no changes in the hydration states of the sulfates in Quartier between the first measurements on sol 293 and the subsequent measurements on sol 304. The identification of $MgSO_4{\cdot}nH_2O$ ($2 < n \leq 5$) at the crater floor and western fan thus implies that these sulfates are in equilibrium with present-day surface environmental conditions, where, based on the phase diagram in Chipera et al. (2023), four-water starkeyite is expected to be the thermodynamically stable phase at the temperature and RH conditions of SHERLOC measurements (∼<3% RH and ∼200–220 K except Guillaumes on sol 161; Section 2.1; Polkko et al., 2023; Siljeström et al., 2024).

Lower hydration Mg-sulfates with 1–2 water are commonly present in the fan, particularly the fan front (Figure 9e and Table 3). The time between abrasion and the last SHERLOC observation of Berry Hollow, where Mg-sulfates with 1–2 water are commonly found, is 9 days. The abrasion patch of Dourbes in Séítah, where Mg-sulfates with 3–5 waters are commonly found, was exposed for a longer period of 16 days. Considering the slow dehydration and rehydration kinetics, the prevalence of low-hydration Mg-sulfates in the fan front is unlikely to be caused by the exposure duration of the abrasion patch.

Kieserite is the thermodynamically stable phase at temperatures above ∼50°C, which is more than 100°C higher than the present-day temperature. While a combination of low thermal inertia and low albedo can cause rocks to reach higher maximum temperatures locally, the sand dunes at Gale crater with low thermal inertia and albedo

were found to only be ∼15°C warmer than sedimentary rocks of higher thermal inertia (Vasavada et al., 2017). The occurrences of Mg-sulfates with 1–2 waters in Jezero crater are thus out of equilibrium with present-day surface environmental conditions, implying that processes that are not thermodynamically and kinetically favored at the surface now are required for their formations (Section 4.7).

4.6. Comparison of SHERLOC Hydration Detections to Orbital Detections and Other Mars 2020 Instruments

While in situ investigation of the Jezero fan and floor rocks with SHERLOC revealed sulfates as the dominant hydration phase across all geologic units, sulfates have not been identified at Jezero crater with orbital spectroscopy. Instead, near-infrared spectroscopy from orbit shows that the Jezero crater floor is dominated by olivine and pyroxene signatures with limited hydration (e.g., Ehlmann et al., 2008, 2009; Goudge et al., 2015; Horgan et al., 2020),while in the fan front and the upper fan, signatures from alteration phases Fe/Mg-smectite clays and carbonates are found widely distributed (Ehlmann et al., 2009; Goudge et al., 2017; Horgan et al., 2020). This discrepancy could be because the areal coverage of the sulfates is insufficient to exhibit a strong signature in orbital spectra. While hydrated sulfates have been observed with SHERLOC in all geologic units, they are not observed in all targets, suggesting limited spatial distribution of sulfates at Jezero crater. Alternatively, the spectral signatures of these low-hydration Mg-sulfates in the Jezero fan could be obscured by the presence of phyllosilicates; laboratory studies show that this occurs for a mixture of amorphous hydrated Mg-sulfate with as little as 10 wt.% smectite (Sheppard et al., 2022). Interestingly, SHERLOC has not identified phyllosilicates in the Jezero fan or floor (Section 4.2). The different mineralogical detections by different instruments at different scales indicate that combining these different data are necessary to properly reconstruct the geological history of an area. It is also important to understand these different mineralogical detections in the context of the sensitivities of each instrument to properly interpret the non-detections of a particular phase.

Only nine SHERLOC targets out of a total of 24 analyzed show detections of hydration peaks (Figure 11). In contrast, all SuperCam LIBS and IRS measurements of these same SHERLOC targets, when they exist, showed evidence for hydration. We can begin to understand the sensitivity of SHERLOC Raman spectroscopy to hydrated phases by examining the hydrated phases detected by SuperCam LIBS and IRS but not SHERLOC. For example, the SuperCam IRS ∼1.9-μm band in the fan front target Novarupta that showed no SHERLOC hydration is attributed to Mg-rich serpentine (Dehouck et al., 2023). Fe/Mg-bearing phyllosilicate such as smectite have also been identified with SuperCam IRS across many targets in the western fan (Dehouck et al., 2023; Mandon et al., 2024). Conversely, the SuperCam IRS spectra of Berry Hollow, a target in the fan front with hydrated sulfates identified with SHERLOC, show lower contribution of phyllosilicate (Dehouck et al., 2023). These results suggest that the SHERLOC Raman spectrometer is sensitive to water in sulfate and less so to other hydrated phases such as Fe/Mg-bearing phyllosilicate, explaining the non-detection by SHERLOC of the phyllosilicates identified from orbit (Section 4.2).

The proportion of SHERLOC hydration detections in Quartier is significantly higher than the others (Figure 11). The averages of the hydration peak areas are also the largest in the Séítah rock Quartier followed by Dourbes. However, the hydration peak areas of individual scan points within the targets vary by orders of magnitude, likely depending on the phase and texture interrogated by the laser shot. For example, in Dourbes the largest hydration peak area is localized within material that is visibly white; points of smaller hydration peak area are found at the edges of this white material. The corresponding sulfate ν_1 peak intensities of these points are also small, suggesting that at the edges, the hydrated sulfates are likely mixed with the surrounding non-hydrated material, resulting in smaller amounts of hydrated sulfates probed by the laser. These results imply that the SHERLOC laser shot needs to hit nearly pure hydrated phases to produce observable hydration signatures in the SHERLOC Raman spectra.

In the targets in the western fan, the hydrated phases are less visibly correlated with observable grains or are mixed with anhydrite. This likely means that the hydrated phases are present at lower concentrations within the SHERLOC 100-μm beam size, thus resulting in the overall smaller values of hydration peak areas. Thus, while the peak positions and shapes of the hydration peaks observed in SHERLOC Raman spectra are useful for identifying the hydrous phase(s) present, the areas of the hydration peaks do not provide meaningful information for understanding the hydration of the bulk rock because the hydration peaks are diminished non-linearly when the concentration of hydrated phases interrogated is low.

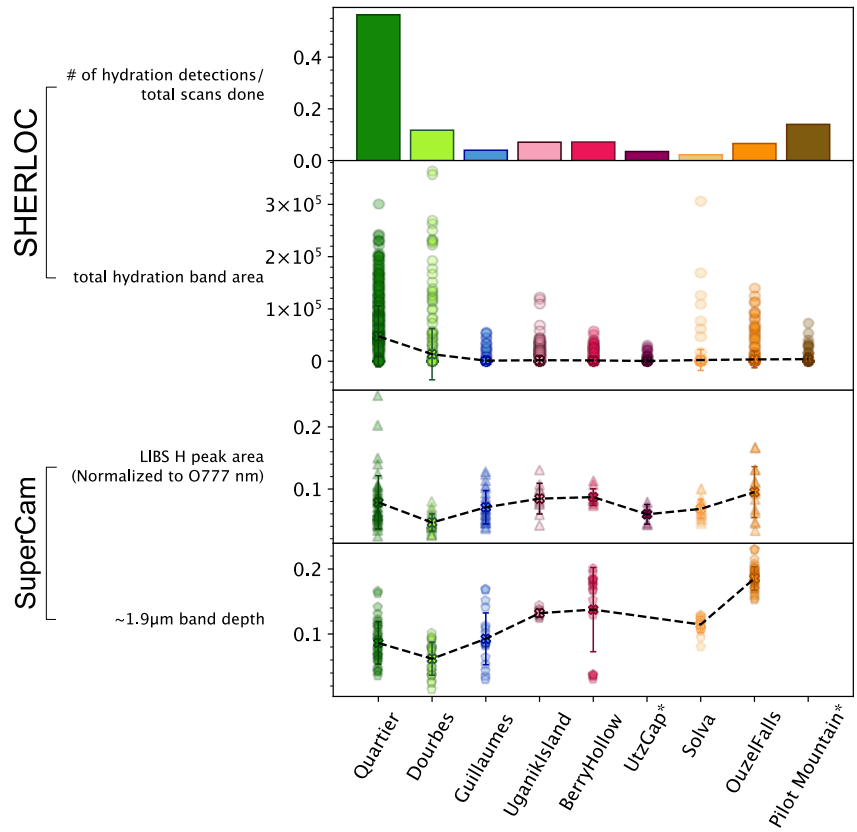

Figure 11. For each target with hydration detections by SHERLOC: (top) Ratio of the number of SHERLOC hydration detections to the total number of SHERLOC scans. (Second) Hydration band area from SHERLOC Raman spectra. (Third) H peak area as measured by SuperCam laser-induced breakdown spectra (LIBS). (Fourth) Band depth of ∼1.9 μm molecular H_2O absorption as measured by SuperCam infrared reflectance spectrometer (IRS). In the bottom three panels, the crosses indicate the mean values of the data plotted, while the error bars indicate ±1 standard deviation of the data plotted. Dashed lines are used to connect the mean values across targets for clarity. *For Utz Gap, the SuperCam LIBS equivalent target was Little Devil's Stairs, a target on the same outcrop, but there is no equivalent target with IRS. There is no equivalent natural surface target measured by SuperCam for Pilot Mountain.

The IRS and LIBS instruments on the SuperCam payload, which also detect hydration signatures, are more indicative of bulk rock hydration. The peak area of the 656-nm H emission line in LIBS and the depth of the ∼1.9-μm band due to the H_2O combination bend and stretch modes in the near-infrared reflectance spectrometer are directly correlated to the water content. In the abrasion patches studied here, LIBS and near-infrared reflectance measurements show that the western fan is equally or more hydrated than the crater floor (Figure 11), corroborated by more observations made by SuperCam on many other targets (e.g., Dehouck et al., 2023; Mandon et al., 2024).

Calibration curves of LIBS H peak area as a function of water content have previously been developed for the ChemCam instrument on the Curiosity rover (Rapin et al., 2017; Thomas et al., 2018, 2020). In this work, we do not provide a quantification of water with the SuperCam instrument, but we investigate hydrogen signal normalized to oxygen following Beck et al. (2023), which should be proportional to water content for solid surfaces, as was shown in Rapin et al. (2017) and Thomas et al. (2018). The data from the Jezero crater for the nine targets that show hydration detections in SHERLOC data are very similar in normalized H peak area (range: 0.02–0.25; mean: 0.07) to the sedimentary rock and soil normalized H peak area from Gale crater (range: 0.02–0.2; mean: ∼0.05; Thomas et al., 2020). If we apply the calibration curves developed for ChemCam, then the range of water content is similar to that measured for the Curiosity rover with most points 1–4 wt.% and a few outliers exceeding 10 wt.%. A caveat is that the SuperCam LIBS instrument on the Mars 2020 rover is different than the ChemCam instrument, and studies are ongoing for the quantification of water content using SuperCam LIBS.

The discrepancy between the trends shown by SHERLOC and SuperCam is likely due to SHERLOC Raman spectrometer being more sensitive to water in sulfate due to its high scattering cross-section and SuperCam IRS and LIBS being equivalently sensitive to sulfates and hydrated silicates. The DUV laser excitation source used in SHERLOC is also readily absorbed by Fe^{3+} cations, leading to lower sensitivity of SHERLOC Raman spectra to hydration and other phases in the presence of Fe-bearing materials. These might cause the targets in the western fan, where hydrated materials are not localized to visible grains and where Fe^{3+}-bearing materials are present (Mandon et al., 2024), to appear less hydrated in the SHERLOC Raman spectra, even though they may contain few wt.% water according to SuperCam. Future lab studies are required to better understand the sensitivities of hydration peaks of Raman spectroscopy in mixture with Mars-relevant materials.

4.7. Environmental Implications

The bulk water content of the SHERLOC hydrated targets, as inferred by comparison of SuperCam LIBS measurements are similar to those of sedimentary rocks at Gale crater, with two points in Quartier exceeding what was measured at Gale crater (Figure 11; Thomas et al., 2020). Opal, Mg-, and Ca-sulfates, phyllosilicates, amorphous silicates and oxyhydroxides are hydrated phases identified at Gale crater (e.g., Chipera et al., 2023; Rapin et al., 2019; Sutter et al., 2017). The hydrated phases in highly altered rocks of ∼20 wt.% water are inferred to be Ca/Mg/Fe-sulfates at Gusev crater (Campbell et al., 2008). Data from SHERLOC similarly suggests that Mg-sulfates are the hydrated phases at the crater floor and western fan of Jezero crater, and Ca-sulfates only at the upper fan. Data from SuperCam IRS show that in addition to sulfates, other hydrated phases are also present at Jezero crater including Fe-oxyhydroxides and Fe/Mg-bearing phyllosilicate such as smectite and vermiculite (Dehouck et al., 2023; Mandon et al., 2023).

No Mg-sulfates of high hydration degrees ($n \geq 6$) have been found at Jezero crater or Gale crater. At Jezero crater, $MgSO_4{\cdot}nH_2O$ ($2 < n \leq 5$) are commonly detected, which are the thermodynamically favored phase(s) for the condition of measurements and are consistent with the detections of starkeyite at Gale crater (e.g., Chipera et al., 2023; Vaniman & Chipera, 2006; Wang et al., 2009; Section 4.5). The occurrence of lower water ($n = 1$–2) Mg-sulfate in the fan is of note and—like kieserite detections from orbit (e.g., Roach et al., 2009) and kieserite detections at Gale crater (Chipera et al., 2023; Tutolo et al., 2024)—demands explanation given that thermodynamics predicts only metastability of this typically high-temperature phase.

While gypsum was identified in veins at Endeavor crater and gypsum, bassanite, and anhydrite at Gale crater (Squyres et al., 2012; Vaniman et al., 2018), the dominant form of Ca-sulfates detected by SHERLOC is anhydrite. Bassanite is detected only at Pilot Mountain of the upper fan while gypsum has not so far been detected by SHERLOC. At Gale crater, bassanite is interpreted to have formed from the dehydration of gypsum and anhydrite likely formed from direct precipitation (Rapin et al., 2016; Vaniman et al., 2018). The direct precipitation of anhydrite commonly occurs at temperatures >50°C, but in fluids with high concentrations of salts, anhydrite can precipitate at temperatures <20°C (Vaniman et al., 2018).

The lack of gypsum, scarcity of bassanite, and pervasiveness of anhydrite detections by SHERLOC at Jezero crater likely indicate that anhydrite formed from direct precipitation. This would either mean that temperatures were >50°C during the formation of Ca-sulfates or that anhydrite precipitated from a highly saline brine. In the latter case, in addition to anhydrite, more soluble salts are expected to precipitate subsequent to anhydrite as the fluid evaporated (Vaniman et al., 2018), which is supported by SHERLOC observations. In the fan front and crater floor of Jezero crater, Ca-sulfates and Mg-sulfates are detected in close proximity (within the same spectra with a beam size of 100 μm or across different scan points few 100 μm apart) in multiple targets. Abundant anhydrous Ca-sulfate and few hydrated Mg-sulfates in the stratigraphically higher fan front contrast with abundant hydrated Mg-sulfate and few anhydrous Ca-sulfates in the stratigraphically lower crater floor, even though there are exceptions such as Bellegarde in the crater floor where only anhydrous Ca-sulfates are detected (Table 3; Siljeström et al., 2024).

The general distributions of Ca- and Mg-sulfates in the Jezero fan and crater floor are surprisingly consistent with a simple model where the Ca- and Mg-sulfates in the fan and crater floor are deposited from the same fluid flowing over the surface (Figure 12). In such a simple model, Ca-sulfates would be preferentially precipitated higher in the stratigraphy at the western fan (step 1 in Figure 12) due to its much lower solubility (0.205 g/100 g H_2O at 25°C; Lide, 2001) than Mg-sulfates (35.7 g/100 g H_2O at 25°C; Lide, 2001; Lide, 2001; Tosca & McLennan, 2006). The more soluble Mg-sulfates are precipitated at the stratigraphically lower crater floor as the

brine evolved and became more concentrated in Mg and sulfate ions, perhaps via evaporation of ponded waters (concurrently with 1. or separately as 2 in Figure 12). This process is similar to that described by Rapin et al. (2019) for Gale crater Ca- and Mg-sulfates. The flow of surface fluid down the stratigraphy is also proposed in Siljeström et al. (2024) to explain the higher occurrences of sulfates in the stratigraphically higher rocks in Séítah. This model would imply that at the time of formation, anhydrite precipitated from a highly saline brine without requiring temperatures >50°C. PIXL elemental analyses of sulfates at the fan front also suggest precipitation of sulfates from highly saline brine (Hurowitz et al., 2023). This simple model (Figure 12), however, does not preclude that a complex series of multiple fluid events with different ionic compositions occurred. The unconformity between the fan and the crater floor (Stack et al., 2024) may also imply breaks in fluid events thus increasing the complexity of multiple events related to precipitation from groundwater percolating through the bedrock.

Siljeström et al. (2024) hypothesized that the highly saline Mg- and sulfate-containing fluid that precipitated sulfates in the crater floor could have originated from the dissolution of sulfates in the western fan. This could be consistent with the lower Mg:Fe cation ratio in the sulfates of the fan front (50:50) than the crater floor (90:10) (Hurowitz et al., 2023; Siljeström et al., 2024). However, in this work, we find that the upper fan has bassanite and, relative to the fan front, fewer contributions of anhydrite, fewer detections of lower hydration Mg-sulfates (n = 1–2), and hydration spectra that show clear bimodal peaks which are more similar to the crater floor hydration spectra (Figures 3, 8 and 9). If these differences in the observed Ca- and Mg-sulfate detections and compositions are not a result of sampling bias, then one possibility is that the Ca-, Mg- and sulfate-containing fluid that flowed across the fan front and crater floor did not affect the upper fan, and its salts are from a different aqueous event(s).

Another possibility is that the Ca-sulfates in the upper fan were formed from the same Ca-, Mg-, and sulfate-containing fluid that flowed across the fan front and crater floor but the Mg-sulfates in the upper fan were formed in a distinct event(s). This is based on the textural observations that Ca-sulfates in both the upper fan and fan front are often observed in mm-sized white veins, crystals or patches which are interpreted as late-stage diagenetic features (Benison et al., 2024) but the hydrated Mg-sulfates in the upper fan do not necessarily show clear textural associations (Table 3). This is unlike the hydrated Mg-sulfates in the crater floor which are localized to visible white crystals or patches rimmed by carbonates (Corpolongo et al., 2023; Siljeström et al., 2024; Wogsland et al., 2023), interpreted to have been precipitated by sulfate-containing fluids filling the voids (Tice et al., 2022). The lack of textural association may mean that they are the products of later precipitation (or dissolution-precipitation reactions within the silicate grains) because these highly soluble Mg-sulfates would have otherwise been dissolved and transported out of the rock. The carbonates in the upper fan also do not show clear textural associations, perhaps suggesting both alteration phases were deposited in the last stages of aqueous activity in the fan (step 3 in Figure 12).

One hypothesis for the detection of bassanite in only the stratigraphically higher upper fan target Pilot Mountain is that gypsum was over time dehydrated to bassanite, similar to the formation pathway proposed for bassanite detected at Gale crater (Rapin et al., 2016; Vaniman et al., 2018). The direct precipitation of bassanite instead of anhydrite can occur at high-temperature (>80°C) and/or high salinity conditions (Ossorio et al., 2014). As we propose that anhydrite in the fan front and crater floor precipitated from a highly saline brine at temperatures lower than 50°C, if bassanite in Pilot Mountain formed from the same Ca-, Mg-, sulfate-containing fluid in one continuous event, it is less likely that bassanite formed from direct precipitation. This is because the low-temperature fluid originating from a stratigraphically higher location would have been less concentrated at the upper fan than the fan front, which would favor the precipitation of gypsum over bassanite or anhydrite. A third possibility to explain the observation of bassanite in Pilot Mountain is that while the same Ca-, Mg-, sulfate-containing fluid flowed across the upper fan, fan front and the crater floor, there were local or temporal changes in fluid composition and temperature that result in target-to-target variation in the Ca- and Mg-sulfate mineral assemblages within units, not only in the upper fan but in the crater floor as well where only anhydrous Ca-sulfate and no hydrated Mg-sulfate is detected in one of the targets Bellegarde (Table 3; Siljeström et al., 2024).

The persistence of the late-stage anhydrite and bassanite to the modern day implies arid conditions. This is also consistent with the absence of detections by SHERLOC of any Mg-sulfates of high hydration degree (>5 water per formula unit); any Mg-sulfates of high hydration degree such as hexahydrite, epsomite or meridianiite have

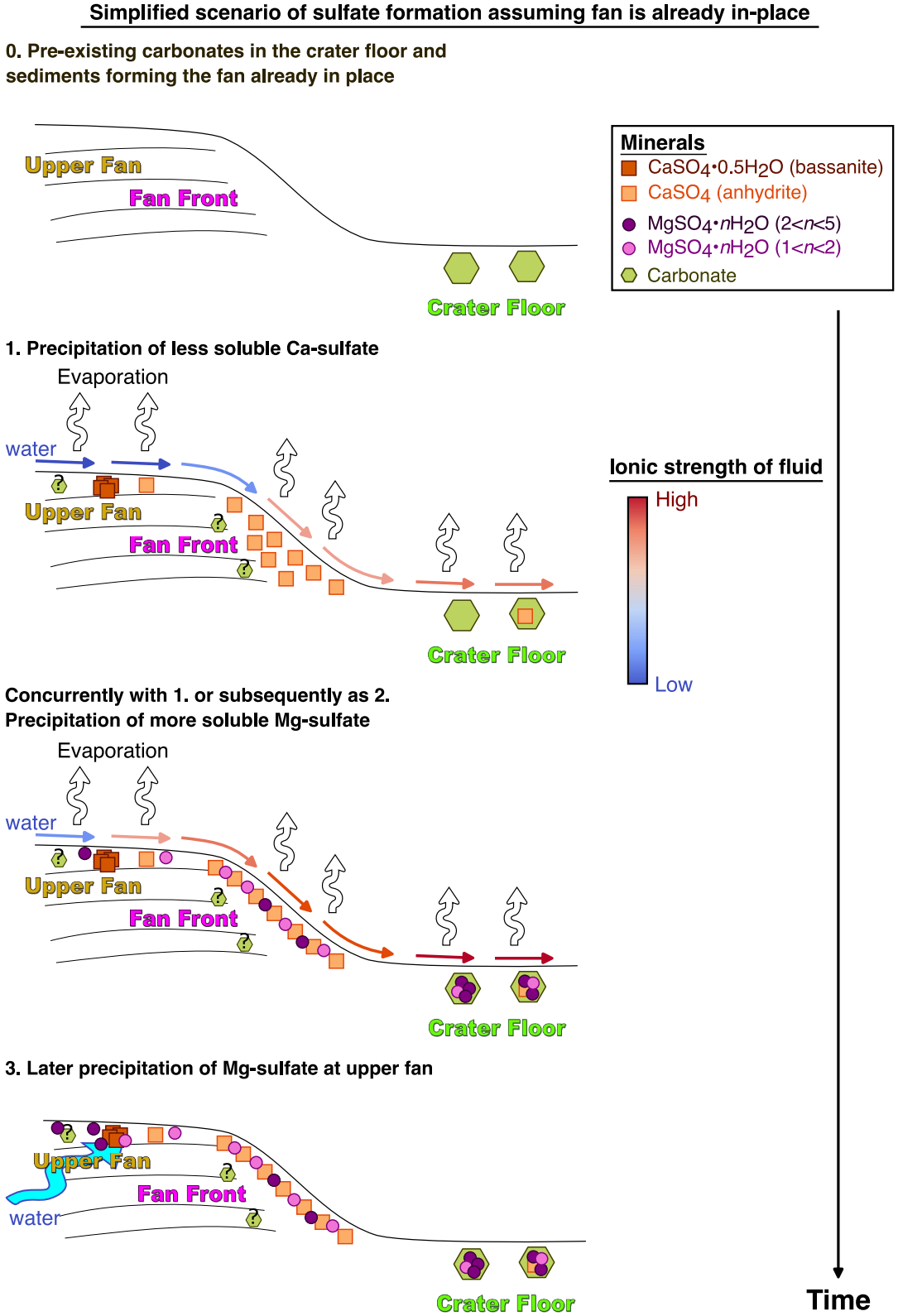

Figure 12.

since dehydrated. The dehydration products expected are starkeyite at temperatures below 50°C and kieserite at temperatures above 50°C (Wang et al., 2009). The detections of anhydrite and kieserite that both require high temperatures to form (>50°C) could mean that there was a heat source particularly at the western fan in Jezero crater.

However, similar to anhydrite, kieserite can also form at low temperatures (<50°C), as a dehydration product or through direct precipitation. Experimental studies have shown that kieserite can form at $T < 69$°C through the dehydration of epsomite when it co-exists with amorphous Mg-sulfates or other sulfates such as Ca-sulfates (Wang et al., 2009). This phenomenon may also occur at lower temperatures because other co-existing phases may enhance the sulfate activity locally at the point of crystal formation. On the other hand, geochemical modeling based on thermodynamics proposed that kieserite can precipitate directly from Cl-enriched brine at 15°C (e.g., Marion et al., 2009). However, experimental studies by Wang et al. (2016) showed no precipitation of kieserite from Cl-enriched brine, and it was suggested that the direct precipitation of kieserite from Cl-enriched brine may be kinetically prohibited. Instead, it is more likely that the formation of kieserite on Mars at low temperatures is driven by the dehydration of high hydration $MgSO_4{\cdot}nH_2O$ ($n = 11, 7, 6$) that coprecipitated with other sulfates and chlorides from Mg, Ca, SO_4, Cl-containing brine (Wang et al., 2016). This is clearly an area needing further laboratory study.

At Jezero crater, Ca-sulfate has been observed to coexist with Mg-sulfates in many targets across the fan and crater floor. Cl-bearing mineral perchlorate has also been detected in the crater floor (Figure 4, Corpolongo et al., 2023; Scheller et al., 2022). The coexistence of sulfate and perchlorate in the Máaz target Guillaumes suggests that sulfate precipitated with perchlorate or other parent Cl-bearing mineral such as halite from a highly saline Mg, Ca, SO_4, Cl-brine (Scheller et al., 2022). Based on the detections of these Ca-sulfate and Cl-bearing phases, we believe that it is more likely that the lower hydration Mg-sulfates with 1–2 waters at Jezero crater formed at mid-temperatures through the dehydration of high hydration $MgSO_4{\cdot}nH_2O$ ($n = 11, 7, 6$), facilitated by coexisting Ca-sulfate or Cl-bearing species, rather than through direct precipitation from Cl-enriched brine. While no Cl-bearing mineral has been definitively identified in the fan, there are more frequent detections of anhydrite as well as larger contributions of anhydrite in some spectra in the fan front than in the crater floor or upper fan (Figure 8). This coexistence of anhydrite is in line with the more prevalent SHERLOC detections of Mg-sulfates of lower hydration degree in the fan front. Collectively, our data underscore the importance of characterizing sulfates with Raman under Martian conditions and understanding the effects of co-existing phases, which can create localized conditions that stabilize Mg-sulfate phases that are thermodynamically out of equilibrium with present-day surface conditions.

5. Conclusions

In order to understand the fluid history in the Jezero crater system and carriers of hydration, we analyzed SHERLOC Raman spectral data of stratigraphically in-place rock targets of the Séítah and Máaz formations of the crater floor and the Shenandoah formation (fan front) and upper fan of the western fan delta. This builds upon previous work by Siljeström et al. (2024) studying hydrated phases in the igneous crater floor. By examination of the shape and position of Raman peaks in the 800–1,200 cm^{-1} (mineral region) and 2,800–3,900 cm^{-1} (hydration region), we found that sulfates are a principal hydration carrier phase in all units. There are four characteristic expressions of hydration: (a) a bimodal spectral feature with peaks at ~3,200 and ~3,400 cm^{-1}, (b) an asymmetric feature that contains a single peak at ~3,400 cm^{-1}, (c) a single Gaussian peak at ~3,400 cm^{-1}, and (d) narrow feature with a peak at ~3,550 cm^{-1} and a higher wavenumber peak not as clearly resolved.

Figure 12. A simplified scenario for sulfate formation assuming pre-existing carbonate in the crater floor, which formed before sulfates (Tice et al., 2022) (0). We reproduce the observed lack of textural association of the carbonates in the upper fan and fan front and Mg-sulfates in the upper fan, the localized nature of the sulfates in the fan front, and the carbonates rimming the sulfates in the crater floor (see Table 3). This endmember scenario starts by assuming that the sediments that formed the fan are already in place (we do not think that this is true and believe that the sedimentology is more complex than depicted here, e.g., Stack et al. (2024)). The precipitation of less soluble Ca-sulfate (1) occurred concurrently with or was followed by the precipitation of more soluble Mg-sulfate (2). Low-hydration Mg-sulfate is found concentrated in the fan front coexisting with anhydrite, which can create localized conditions that stabilize low-hydration Mg-sulfate. Then a later period of water activity precipitated low- and/or high-hydration Mg-sulfates in the upper fan (3). Carbonates in the fan front and upper fan are labeled with "?" because we are not able to constrain the relative timing of carbonate formation in the fan based on SHERLOC Raman spectral data alone.

From comparison of laboratory data to these hydration peaks in conjunction with sulfate peaks in the mineral region, we determined the specific sulfates present in terms of cation and hydration state and that these varied by geological unit. Abundant anhydrous Ca-sulfate and fewer occurrences of hydrated Mg-sulfates in the stratigraphically higher fan front contrasts with abundant hydrated Mg-sulfates and few anhydrous Ca-sulfates in the stratigraphically lower crater floor. $MgSO_4{\cdot}nH_2O$ ($2 < n \leq 5$) is a likely hydration carrier phase in all units (~1,000–1,025 cm^{-1} sulfate peak and 3,400 cm^{-1} hydration peak), but Mg-sulfates of lower hydration degree ($n = 1$–2; >1,025 cm^{-1} sulfate peak and 3,400 cm^{-1} hydration peak) are more commonly found in the fan than the crater floor. Hydrated Ca-sulfates (>3,500 cm^{-1} hydration peak) are found only at the upper fan, while anhydrite is found in all units. We have not been able to definitively attribute hydration peaks at ~3,200 cm^{-1}, but a possibility is low-hydration amorphous Mg-sulfates ($n \leq 1$). Carbonates are commonly found to co-occur with sulfates, with more Fe-rich carbonates found on the crater floor and more Mg-rich carbonates on the fan. Further laboratory characterizations of the hydrated Mg-sulfate system and mixtures at Mars-relevant conditions are essential to more definitively interpret the SHERLOC Raman spectra. The variability in alteration and hydrated mineralogy across the crater floor and western fan indicate that a diverse range of fluid environments existed in the past at Jezero crater. These observations are consistent with a simple model where Ca-sulfates in the floor and fan are preferentially precipitated higher in the stratigraphy in the western fan due to their lower solubility, and the more soluble Mg-sulfates are precipitated at the stratigraphically lower crater floor due to evaporative concentration. Anhydrite and kieserite likely signify high ionic strength fluids rather than temperatures >50°C. The ionic strength of this fluid would likely have been lower in the stratigraphically higher upper fan, precipitating hydrated Ca-sulfate gypsum instead of anhydrite, and which subsequently dehydrated to bassanite. Later aqueous episodes may be responsible for the dissemination of Mg-sulfates within the sedimentary rocks in the fan. Collectively, the data imply aqueous deposition of sediments with contemporaneous or subsequent formation of salts, and subsequent aridity to preserve the observed hydration states.

Appendix A: SNR Calculation Approaches and Result Sensitivity

Determination of the significance threshold of detected peaks in spectra requires choice of metric and different authors have adopted distinct computational methods for calculation of the noise, peak height, and number of channels. In this work, we assess the presence of signal for both mineral peaks that are narrow with high intensity and hydration peaks that are broad with low intensity. We have used peak height metrics to determine peak detections. While the band area, and thus total signal, of the two types of mineral and hydration peaks may be similar, the hydration peaks have a lower probability of detection because of their low intensity and large widths. To ensure that we are adequately detecting both peak types, we have examined the sensitivity of results to three methods of calculating signal-to-noise ratio (SNR) and present the sensitivity of peak detections to the SNR metric chosen:

1. SNR is defined as the intensity of the fitted peak, divided by the standard deviation of noise across 2,000–2,100 cm^{-1}. SNR > 2 was set as the threshold, as described in Section 2.5. This was adopted for the main text.
2. SNR is defined as the average peak height of raw data above the background calculated across 5 pixels to the left and right of the central pixel, divided by the standard deviation of noise across 2,000–2,100 cm^{-1}. SNR > 2 was set as the threshold.
3. Lenz and Ayres (1992) express a general scaling relationship of the SNR of a fitted peak of a Gaussian profile as a function of the number of channels sampled to account for the fact that multiple channels contribute to the peak:

$$\mathrm{SNR} = C \times \left(\frac{\mathrm{FWHM}}{\Delta\lambda}\right)^{1/2} \times \frac{f_0}{\langle\sigma_i\rangle}$$

where C is a proportionality constant, $\Delta\lambda$ is the width of one channel, which is 9 cm^{-1} in the case of SHERLOC Raman spectrometer, f_0 is the intensity of the central pixel and $\langle\sigma_i\rangle$ is the mean noise level. The proportionality constant is given as 0.70 in Lenz and Ayres (1992) for the case where the noise is a constant independent of the intensity, which is relevant to SHERLOC Raman spectra where we have calculated $\langle\sigma_i\rangle$ to be the standard deviation of noise across 2,000–2,100 cm^{-1}. SNR > 3 was set as the threshold as this method takes into account the whole peak profile so there is no need to artificially lower the threshold for broad but low intensity peaks such as

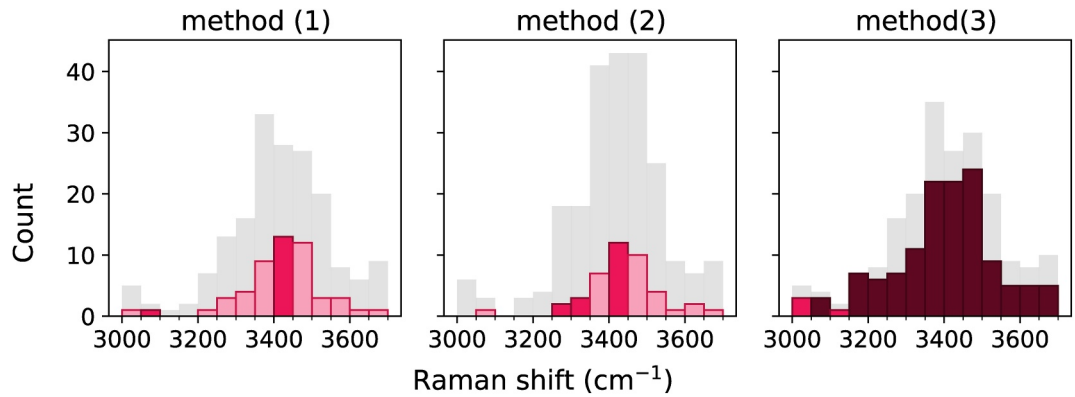

Figure A1. Histogram plots of hydration peaks detected in Berry Hollow, based on signal-to-noise ratio (SNR) calculations of methods (1)–(3) outlined in the text. Bin size = 50 cm^{-1}. Gray bars represent average SNR > 1, light-colored bars represent peaks of 2 < average SNR ≤ 3, medium colored bars represent peaks of 3 < average SNR ≤ 5, dark colored bars represent peaks of average SNR > 5.

the hydration peaks. This scaling relation samples across the whole band profile, and necessarily produces SNR greater than the SNR based on peak height for many hydration peaks observed in the SHERLOC Raman spectra where FWHM ≫ $\Delta\lambda$.

The total number of peaks detected at each Raman shift position in the hydration region for methods (1)–(3) is shown in Figure A1, using Berry Hollow as an example.

The proportion of the number of peaks above the threshold of SNR > 2 (for methods (1) and (2)) or SNR > 3 (for methods (3)) to the number of peaks of SNR > 1 is 0.29, 0.19, and 0.65 for methods (1)–(3) respectively. The total number of peak detections is increased in method (3) as expected due to the proportionality to the FWHM in method (3), which can be as large as 300 cm^{-1} in the hydration region. While statistically the location of the modal peak center is similar across method (1)–(3), the number of spectra classified as hydrated change depending on the choice of SNR metric. In the main text of this work, we have used only method (1) to calculate the SNR.

Data Availability Statement

All SHERLOC mission data described in this manuscript are accessible through the NASA Planetary Data System (PDS) archive (Beegle & Bhartia, 2021). Data used here were sourced from the "Raw Spectroscopy" data collection. Specifically, data files with the ERA, ERB, ESP, and EPA product IDs were used as source files. The ACI and WATSON images were sourced from the PDS archive ACI image data and WATSON image data collections, respectively. EDR and ECM products were used. The CDR LIBS and reflectance spectra from SuperCam are available on the PDS (Maurice & Wiens, 2021). Loupe software (Uckert, 2022) was used to export SHERLOC data, which was subsequently processed using Python and related open-source Python libraries. Processed data used in constructing figures including peak fitting results of SHERLOC Raman spectra, SuperCam LIBS H peak area, and SuperCam IRS 1900 nm band depth, as well as spectral data of anhydrite and kieserite measured in this work are available at the CaltechDATA site (Phua et al., 2024).

Acknowledgments
We thank the SHERLOC and Mars 2020 science and engineering teams for the data that enabled this study. This research was supported by funds to the SHERLOC instrument team and the NASA Mars 2020 mission. Y.P. and B.L.E. were supported by a Mars-2020 SHERLOC Co-Investigator grant to B.L.E. S.Si. acknowledges funding from the Swedish National Space Agency (contract 2021-00092 and 137/19). A.D.C. was supported by the Mars 2020 Returned Sample Science Participating Scientist Program (NASA award number 80NSSC20K0237). Support for R.C.W. and S.C. was provided by a SHERLOC Co-Investigator grant to R.C.W. and by NASA contract NNH13ZDA018O. Funding for R.S.J. was provided as an Advanced Curation project run by the NASA Astromaterials Acquisition and Curation Office, Johnson Space Center under the Jacobs, JETSII contract. MPZ was supported by Grant PID2022-140180OB-C21 funded by MCIN/AEI/10.13039/501100011033/ FEDER, UE. Research efforts carried out at the Jet Propulsion Laboratory, California Institute of Technology by K. H., S.Sh., K.U. were funded under a contract with the National Aeronautics and Space Administration (80NM0018D0004). L.M. was supported by a Texaco Postdoctoral prize fellowship awarded by the division of Geological and Planetary Sciences of Caltech.

References

Ballirano, P., & Melis, E. (2009). The thermal behaviour of γ-$CaSO_4$. *Physics and Chemistry of Minerals*, *36*(6), 319–327. https://doi.org/10.1007/s00269-008-0280-0

Beck, P., Forni, O., Dehouck, E., Beyssac, O., Benzerara, K., Quantin-Nataf, C., et al. (2023). Secondary mineralogy of Jezero delta rocks from hydrogen and carbon emission lines in SuperCam LIBS data. In *Paper presented at the 54th lunar and planetary science conference (LPSC)*. Retrieved from https://www.hou.usra.edu/meetings/lpsc2023/pdf/1241.pdf

Beegle, L. W., & Bhartia, R. (2021). *Mars 2020 SHERLOC bundle*. NASA Planetary Data System. https://doi.org/10.17189/1522643

Benison, K. C., Gill, K. K., Sharma, S., Siljeström, S., Zawaski, M., Bosak, T., et al. (2024). Depositional and diagenetic sulfates of Hogwallow flats and Yori Pass, Jezero Crater: Evaluating preservation potential of environmental indicators and possible biosignatures from past Martian surface waters and groundwaters. *Journal of Geophysical Research: Planets*, *129*(2), e2023JE008155. https://doi.org/10.1029/2023JE008155

Bhartia, R., Beegle, L. W., DeFlores, L., Abbey, W., Razzell Hollis, J., Uckert, K., et al. (2021). Perseverance's scanning habitable environments with Raman and Luminescence for Organics and Chemicals (SHERLOC) investigation. *Space Science Reviews*, *217*(4), 58. https://doi.org/10.1007/s11214-021-00812-z

Bibring, J.-P., Langevin, Y., Mustard, J. F., Poulet, F., Arvidson, R., Gendrin, A., et al. (2006). Global mineralogical and aqueous Mars history derived from OMEGA/Mars express data. *Science*, *312*(5772), 400–404. https://doi.org/10.1126/science.1122659

Bristow, T. F., Bish, D. L., Vaniman, D. T., Morris, R. V., Blake, D. F., Grotzinger, J. P., et al. (2015). The origin and implications of clay minerals from Yellowknife Bay, Gale crater, Mars. *American Mineralogist*, *100*(4), 824–836. https://doi.org/10.2138/am-2015-5077CCBYNCND

Bristow, T. F., Rampe, E. B., Achilles, C. N., Blake, D. F., Chipera, S. J., Craig, P., et al. (2018). Clay mineral diversity and abundance in sedimentary rocks of Gale crater, Mars. *Science Advances*, *4*(6), eaar3330. https://doi.org/10.1126/sciadv.aar3330

Buzgar, N., & Apopei, A. I. (2009). The Raman study of certain carbonates. *Geologie*, *55*(2), 97–112. https://doi.org/10.13140/2.1.1358.3368

Califano, S., & Schettino, V. (1988). Vibrational relaxation in molecular crystals. *International Reviews in Physical Chemistry*, *7*(1), 19–57. https://doi.org/10.1080/01442358809353204

Campbell, J. L., Gellert, R., Lee, M., Mallett, C. L., Maxwell, J. A., & O'Meara, J. M. (2008). Quantitative in situ determination of hydration of bright high-sulfate Martian soils. *Journal of Geophysical Research*, *113*(E6), E06S11. https://doi.org/10.1029/2007JE002959

Chio, C. H., Sharma, S. K., & Muenow, D. W. (2004). Micro-Raman studies of gypsum in the temperature range between 9 K and 373 K. *American Mineralogist*, *89*(2–3), 390–395. https://doi.org/10.2138/am-2004-2-320

Chio, C. H., Sharma, S. K., & Muenow, D. W. (2005). Micro-Raman studies of hydrous ferrous sulfates and jarosites. *Spectrochimica Acta Part A: Molecular and Biomolecular Spectroscopy*, *61*(10), 2428–2433. https://doi.org/10.1016/j.saa.2005.02.021

Chipera, S. J., Vaniman, D. T., Rampe, E. B., Bristow, T. F., Martínez, G., Tu, V. M., et al. (2023). Mineralogical investigation of Mg-sulfate at the Canaima drill site, Gale Crater, Mars. *Journal of Geophysical Research: Planets*, *128*(11), e2023JE008041. https://doi.org/10.1029/2023JE008041

Clark, B. C., Morris, R. V., McLennan, S. M., Gellert, R., Jolliff, B., Knoll, A. H., et al. (2005). Chemistry and mineralogy of outcrops at Meridiani Planum. *Earth and Planetary Science Letters*, *240*(1), 73–94. https://doi.org/10.1016/j.epsl.2005.09.040

Clark, J. V., Morris, R. V., Haney, N. C., Jakubek, R. S., Archer, P. D., McAdam, A. C., et al. (2023). Combined thermal and evolved gas analysis, X-ray diffraction, VIS-NIR, X-ray fluorescence, and DUV Raman spectroscopy of synthetic amorphous magnesium sulfates and starkeyite: Implications for the detection of Mg sulfates by the sample analysis at Mars instrument in Gale crater, Mars. In *Paper presented at the 54th lunar and planetary science conference (LPSC)*. Retrieved from https://www.hou.usra.edu/meetings/lpsc2023/pdf/2441.pdf

Clavé, E., Benzerara, K., Meslin, P.-Y., Forni, O., Royer, C., Mandon, L., et al. (2023). Carbonate detection with SuperCam in igneous rocks on the floor of Jezero Crater, Mars. *Journal of Geophysical Research: Planets*, *128*(6), e2022JE007463. https://doi.org/10.1029/2022JE007463

Coleyshaw, E. E., Crump, G., & Griffith, W. P. (2003). Vibrational spectra of the hydrated carbonate minerals ikaite, monohydrocalcite, lansfordite and nesquehonite. *Spectrochimica Acta Part A: Molecular and Biomolecular Spectroscopy*, *59*(10), 2231–2239. https://doi.org/10.1016/S1386-1425(03)00067-2

Corpolongo, A., Jakubek, R. S., Burton, A. S., Brown, A. J., Yanchilina, A., Czaja, A. D., et al. (2023). SHERLOC Raman mineral class detections of the Mars 2020 crater floor campaign. *Journal of Geophysical Research: Planets*, *128*(3), e2022JE007455. https://doi.org/10.1029/2022JE007455

Dehouck, E., Forni, O., Quantin-Nataf, C., Beck, P., Mangold, N., Royer, C., et al. (2023). Overview of the bedrock geochemistry and mineralogy observed by SuperCam during Perseverance's delta front campaign. In *Paper presented at the 54th lunar and planetary science conference (LPSC)*. Retrieved from https://www.hou.usra.edu/meetings/lpsc2023/pdf/2862.pdf

Ehlmann, B. L., Mustard, J. F., Fassett, C. I., Schon, S. C., Head, J. W., III, Des Marais, D. J., et al. (2008). Clay minerals in delta deposits and organic preservation potential on Mars. *Nature Geoscience*, *1*(6), 355–358. https://doi.org/10.1038/ngeo207

Ehlmann, B. L., Mustard, J. F., Swayze, G. A., Clark, R. N., Bishop, J. L., Poulet, F., et al. (2009). Identification of hydrated silicate minerals on Mars using MRO-CRISM: Geologic context near Nili Fossae and implications for aqueous alteration. *Journal of Geophysical Research*, *114*(E2), E00D08. https://doi.org/10.1029/2009JE003339

Farley, K. A., Stack, K. M., Shuster, D. L., Horgan, B. H. N., Hurowitz, J. A., Tarnas, J. D., et al. (2022). Aqueously altered igneous rocks sampled on the floor of Jezero crater, Mars. *Science*, *377*(6614), eabo2196. https://doi.org/10.1126/science.abo2196

Farley, K. A., Williford, K. H., Stack, K. M., Bhartia, R., Chen, A., de la Torre, M., et al. (2020). Mars 2020 mission overview. *Space Science Reviews*, *216*(8), 142. https://doi.org/10.1007/s11214-020-00762-y

Fassett, C. I., & Head III, J. W. (2005). Fluvial sedimentary deposits on Mars: Ancient deltas in a crater lake in the Nili Fossae region. *Geophysical Research Letters*, *32*(14), L14201. https://doi.org/10.1029/2005GL023456

Finocchiaro, C., Coccato, A., Barone, G., Bersani, D., Culka, A., Fornasini, L., et al. (2022). In situ and micro-Raman spectroscopy for the identification of natural Sicilian zeolites. *Journal of Raman Spectroscopy*, *53*(3), 525–539. https://doi.org/10.1002/jrs.6278

Fouchet, T., Reess, J.-M., Montmessin, F., Hassen-Khodja, R., Nguyen-Tuong, N., Humeau, O., et al. (2022). The SuperCam infrared spectrometer for the perseverance rover of the Mars2020 mission. *Icarus*, *373*, 114773. https://doi.org/10.1016/j.icarus.2021.114773

Fox, V. K., Kupper, R. J., Ehlmann, B. L., Catalano, J. G., Razzell-Hollis, J., Abbey, W. J., et al. (2021). Synthesis and characterization of Fe(III)-Fe(II)-Mg-Al smectite solid solutions and implications for planetary science. *American Mineralogist*, *106*(6), 964–982. https://doi.org/10.2138/am-2020-7419CCBYNCND

Fries, M. D., Lee, C., Bhartia, R., Razzell Hollis, J., Beegle, L. W., Uckert, K., et al. (2022). The SHERLOC calibration target on the Mars 2020 perseverance rover: Design, operations, outreach, and future human exploration functions. *Space Science Reviews*, *218*(6), 46. https://doi.org/10.1007/s11214-022-00907-1

Goudge, T. A., Milliken, R. E., Head, J. W., Mustard, J. F., & Fassett, C. I. (2017). Sedimentological evidence for a deltaic origin of the western fan deposit in Jezero crater, Mars and implications for future exploration. *Earth and Planetary Science Letters*, *458*, 357–365. https://doi.org/10.1016/j.epsl.2016.10.056

Goudge, T. A., Mustard, J. F., Head, J. W., Fassett, C. I., & Wiseman, S. M. (2015). Assessing the mineralogy of the watershed and fan deposits of the Jezero crater paleolake system, Mars. *Journal of Geophysical Research: Planets*, *120*(4), 775–808. https://doi.org/10.1002/2014JE004782

Haskin, L. A., Wang, A., Rockow, K. M., Jolliff, B. L., Korotev, R. L., & Viskupic, K. M. (1997). Raman spectroscopy for mineral identification and quantification for in situ planetary surface analysis: A point count method. *Journal of Geophysical Research*, *102*(E8), 19293–19306. https://doi.org/10.1029/97JE01694

Horgan, B. H. N., Anderson, R. B., Dromart, G., Amador, E. S., & Rice, M. S. (2020). The mineral diversity of Jezero crater: Evidence for possible lacustrine carbonates on Mars. *Icarus*, *339*, 113526. https://doi.org/10.1016/j.icarus.2019.113526

Hurowitz, J., Tice, M. M., Allwood, A. C., Cable, M. L., Bosak, T., Broz, A., et al. (2023). The petrogenic history of the Jezero crater delta front from microscale observations by the Mars 2020 PIXL instrument. In *Paper presented at the 54th lunar and planetary science conference (LPSC)*. Retrieved from https://www.hou.usra.edu/meetings/lpsc2023/pdf/2301.pdf

Jakubek, R. S., Bhartia, R., Uckert, K., Asher, S. A., Czaja, A. D., Fries, M. D., et al. (2023). Calibration of Raman bandwidths on the scanning habitable environments with Raman and luminescence for Organics and Chemicals (SHERLOC) deep ultraviolet Raman and fluorescence instrument aboard the perseverance rover. *Applied Spectroscopy*. https://doi.org/10.1177/00037028231210885

Lafuente, B., Downs, R. T., Yang, H., & Stone, N. (2015). The power of databases: The RRUFF project. In T. Armbruster & R. M. Danisi (Eds.), *Highlights in mineralogical crystallography* (pp. 1–30). W. De Gruyter.

Leikin, S., Parsegian, V. A., Yang, W.-H., & Walrafen, G. E. (1997). Raman spectral evidence for hydration forces between collagen triple helices. *Proceedings of the National Academy of Sciences of the United States of America*, *94*(21), 11312–11317. https://doi.org/10.1073/pnas.94.21.11312

Lenz, D. D., & Ayres, T. R. (1992). Errors associated with fitting Gaussian profiles to noisy emission-line spectra. *Publications of the Astronomical Society of the Pacific*, *104*(681), 1104. https://doi.org/10.1086/133096

Lichtenberg, K. A., Arvidson, R. E., Poulet, F., Morris, R. V., Knudson, A., Bell, J. F., et al. (2007). Coordinated analyses of orbital and Spirit Rover data to characterize surface materials on the cratered plains of Gusev Crater, Mars. *Journal of Geophysical Research*, *112*(E12), E12S90. https://doi.org/10.1029/2006JE002850

Lide, D. R. (2001). *CRC handbook of chemistry and physics* (85th ed.). CRC Press.

Ling, Z. C., & Wang, A. (2010). A systematic spectroscopic study of eight hydrous ferric sulfates relevant to Mars. *Icarus*, *209*(2), 422–433. https://doi.org/10.1016/j.icarus.2010.05.009

Liu, Y., Tice, M. M., Schmidt, M. E., Treiman, A. H., Kizovski, T. V., Hurowitz, J. A., et al. (2022). An olivine cumulate outcrop on the floor of Jezero crater, Mars. *Science*, *377*(6614), 1513–1519. https://doi.org/10.1126/science.abo2756

Lopez-Reyes, G., Nachon, M., Veneranda, M., Beyssac, O., Madariaga, J. M., Manrique, J. A., et al. (2023). Anhydrite detections by Raman spectroscopy with SuperCam at the Jezero delta, Mars. In *Paper presented at the 54th lunar and planetary science conference (LPSC)*. Retrieved from https://www.hou.usra.edu/meetings/lpsc2023/pdf/1721.pdf

Mandon, L., Ehlmann, B. L., Wiens, R. C., & Garczynski, B. J. (2024). Variable past redox conditions at Jezero crater, Mars. *Journal of Geophysical Research: Planets*, *129*(7), 2023JE008254. https://doi.org/10.1029/2023JE008254

Mandon, L., Quantin-Nataf, C., Royer, C., Beck, P., Fouchet, T., Johnson, J. R., et al. (2023). Reflectance of Jezero Crater floor: 2. Mineralogical interpretation. *Journal of Geophysical Research: Planets*, *128*(7), e2022JE007450. https://doi.org/10.1029/2022JE007450

Manrique, J. A., Lopez-Reyes, G., Cousin, A., Rull, F., Maurice, S., Wiens, R. C., et al. (2020). SuperCam calibration targets: Design and development. *Space Science Reviews*, *216*(8), 138. https://doi.org/10.1007/s11214-020-00764-w

Marion, G. M., Crowley, J. K., Thomson, B. J., Kargel, J. S., Bridges, N. T., Hook, S. J., et al. (2009). Modeling aluminum–silicon chemistries and application to Australian acidic playa lakes as analogues for Mars. *Geochimica et Cosmochimica Acta*, *73*(11), 3493–3511. https://doi.org/10.1016/j.gca.2009.03.013

Martínez, G. M., Sebastián, E., Vicente-Retortillo, A., Smith, M. D., Johnson, J. R., Fischer, E., et al. (2023). Surface energy budget, albedo, and thermal inertia at Jezero Crater, Mars, as observed from the Mars 2020 MEDA instrument. *Journal of Geophysical Research: Planets*, *128*(2), e2022JE007537. https://doi.org/10.1029/2022JE007537

Maurice, S., & Wiens, R. C. (2021). *Mars 2020 SuperCam bundle*. NASA Planetary Data System. https://doi.org/10.17189/1522646

Maurice, S., Wiens, R. C., Bernardi, P., Caïs, P., Robinson, S., Nelson, T., et al. (2021). The SuperCam instrument suite on the Mars 2020 rover: Science objectives and mast-unit description. *Space Science Reviews*, *217*(3), 47. https://doi.org/10.1007/s11214-021-00807-w

Moeller, R. C., Jandura, L., Rosette, K., Robinson, M., Samuels, J., Silverman, M., et al. (2021). The sampling and caching subsystem (SCS) for the scientific exploration of Jezero Crater by the Mars 2020 perseverance rover. *Space Science Reviews*, *217*(1), 5. https://doi.org/10.1007/s11214-020-00783-7

Morris, R. V., Klingelhöfer, G., Schröder, C., Rodionov, D. S., Yen, A., Ming, D. W., et al. (2006). Mössbauer mineralogy of rock, soil, and dust at Gusev crater, Mars: Spirit's journey through weakly altered olivine basalt on the plains and pervasively altered basalt in the Columbia Hills. *Journal of Geophysical Research*, *111*(E2), E00A16-1. https://doi.org/10.1029/2005JE002584

Mukamel, S. (1985). Stochastic theory of resonance Raman line shapes of polyatomic molecules in condensed phases. *The Journal of Chemical Physics*, *82*(12), 5398–5408. https://doi.org/10.1063/1.448623

Murchie, S. L., Mustard, J. F., Ehlmann, B. L., Milliken, R. E., Bishop, J. L., McKeown, N. K., et al. (2009). A synthesis of Martian aqueous mineralogy after 1 Mars year of observations from the Mars Reconnaissance Orbiter. *Journal of Geophysical Research*, *114*(E2), E00D06. https://doi.org/10.1029/2009JE003342

Ossorio, M., Van Driessche, A. E. S., Pérez, P., & García-Ruiz, J. M. (2014). The gypsum–anhydrite paradox revisited. *Chemical Geology*, *386*, 16–21. https://doi.org/10.1016/j.chemgeo.2014.07.026

Phua, Y., Ehlmann, B. L., Siljeström, S., Czaja, A. D., Beck, P., Connell, S., et al. (2024). Data accompanying "characterizing hydrated sulfates and altered phases in Jezero Crater Fan and floor geologic units with SHERLOC on Mars 2020" [Dataset]. *CaltechDATA*. https://doi.org/10.22002/camz1-c7675

Polkko, J., Hieta, M., Harri, A.-M., Tamppari, L., Martínez, G., Viúdez-Moreiras, D., et al. (2023). Initial results of the relative humidity observations by MEDA instrument onboard the Mars 2020 perseverance rover. *Journal of Geophysical Research: Planets*, *128*(2), e2022JE007447. https://doi.org/10.1029/2022JE007447

Preturlan, J. G. D., Vieille, L., Quiligotti, S., & Favergeon, L. (2019). Comprehensive thermodynamic study of the calcium sulfate–water vapor system. Part 1: Experimental measurements and phase equilibria. *Industrial & Engineering Chemistry Research*, *58*(22), 9596–9606. https://doi.org/10.1021/acs.iecr.9b00856

Prieto-Taboada, N., Gómez-Laserna, O., Martínez-Arkarazo, I., Olazabal, M. Á., & Madariaga, J. M. (2014). Raman spectra of the different phases in the $CaSO_4$–H_2O system. *Analytical Chemistry*, *86*(20), 10131–10137. https://doi.org/10.1021/ac501932f

Qi, X., Ling, Z., Liu, P., Chen, J., Cao, H., Liu, C., et al. (2023). Quantitative mineralogy of planetary silicate ternary mixtures using Raman spectroscopy. *Earth and Space Science*, *10*(5), e2023EA002825. https://doi.org/10.1029/2023EA002825

Rampe, E. B., Blake, D. F., Bristow, T. F., Ming, D. W., Vaniman, D. T., Morris, R. V., et al. (2020). Mineralogy and geochemistry of sedimentary rocks and eolian sediments in Gale crater, Mars: A review after six Earth years of exploration with curiosity. *Geochemistry*, *80*(2), 125605. https://doi.org/10.1016/j.chemer.2020.125605

Rampe, E. B., Ming, D. W., Blake, D. F., Bristow, T. F., Chipera, S. J., Grotzinger, J. P., et al. (2017). Mineralogy of an ancient lacustrine mudstone succession from the Murray formation, Gale crater, Mars. *Earth and Planetary Science Letters*, *471*, 172–185. https://doi.org/10.1016/j.epsl.2017.04.021

Rapin, W., Chauviré, B., Gabriel, T. S. J., McAdam, A. C., Ehlmann, B. L., Hardgrove, C., et al. (2018). In situ analysis of opal in Gale Crater, Mars. *Journal of Geophysical Research: Planets*, *123*(8), 1955–1972. https://doi.org/10.1029/2017JE005483

Rapin, W., Ehlmann, B. L., Dromart, G., Schieber, J., Thomas, N. H., Fischer, W. W., et al. (2019). An interval of high salinity in ancient Gale crater lake on Mars. *Nature Geoscience*, *12*(11), 889–895. https://doi.org/10.1038/s41561-019-0458-8

Rapin, W., Meslin, P.-Y., Maurice, S., Vaniman, D., Nachon, M., Mangold, N., et al. (2016). Hydration state of calcium sulfates in Gale crater, Mars: Identification of bassanite veins. *Earth and Planetary Science Letters*, *452*, 197–205. https://doi.org/10.1016/j.epsl.2016.07.045

Rapin, W., Meslin, P.-Y., Maurice, S., Wiens, R. C., Laporte, D., Chauviré, B., et al. (2017). Quantification of water content by laser induced breakdown spectroscopy on Mars. *Spectrochimica Acta Part B: Atomic Spectroscopy*, *130*, 82–100. https://doi.org/10.1016/j.sab.2017.02.007

Razzell Hollis, J., Abbey, W., Beegle, L. W., Bhartia, R., Ehlmann, B. L., Miura, J., et al. (2021). A deep-ultraviolet Raman and Fluorescence spectral library of 62 minerals for the SHERLOC instrument onboard Mars 2020. *Planetary and Space Science*, *209*, 105356. https://doi.org/10.1016/j.pss.2021.105356

Razzell Hollis, J., Rheingold, D., Bhartia, R., & Beegle, L. W. (2020). An optical model for quantitative Raman microspectroscopy. *Applied Spectroscopy*, *74*(6), 684–700. https://doi.org/10.1177/0003702819895299

Rividi, N., van Zuilen, M., Philippot, P., Ménez, B., Godard, G., & Poidatz, E. (2010). Calibration of carbonate composition using micro-Raman analysis: Application to planetary surface exploration. *Astrobiology*, *10*(3), 293–309. https://doi.org/10.1089/ast.2009.0388

Roach, L. H., Mustard, J. F., Murchie, S. L., Bibring, J.-P., Forget, F., Lewis, K. W., et al. (2009). Testing evidence of recent hydration state change in sulfates on Mars. *Journal of Geophysical Research*, *114*(E2), E00D02. https://doi.org/10.1029/2008JE003245

Royer, C., Fouchet, T., Mandon, L., Montmessin, F., Poulet, F., Forni, O., et al. (2023). Reflectance of Jezero Crater floor: 1. Data processing and calibration of the infrared spectrometer (IRS) on SuperCam. *Journal of Geophysical Research: Planets*, *128*(1), e2022JE007481. https://doi.org/10.1029/2022JE007481

Royer, C., Wiens, R. C., Dehouck, E., Beck, P., Quantin-Nataf, C., Mandon, L., et al. (2023). The mineralogical diversity of Jezero's western fan revealed by SuperCam/IRS, perseverance rover, and spectral modeling. In *Paper presented at the AGU annual meeting 2023, P41E-3222*. Retrieved from https://agu.confex.com/agu/fm23/meetingapp.cgi/Paper/1383783

Santos, J. C. C., Negreiros, F. R., Pedroza, L. S., Dalpian, G. M., & Miranda, P. B. (2018). Interaction of water with the gypsum (010) surface: Structure and Dynamics from nonlinear vibrational spectroscopy and Ab Initio molecular Dynamics. *Journal of the American Chemical Society*, *140*(49), 17141–17152. https://doi.org/10.1021/jacs.8b09907

Sapers, H. M., Razzell Hollis, J., Bhartia, R., Beegle, L. W., Orphan, V. J., & Amend, J. P. (2019). The cell and the sum of its parts: Patterns of complexity in biosignatures as revealed by deep UV Raman spectroscopy. *Frontiers in Microbiology*, *10*, 679. https://doi.org/10.3389/fmicb.2019.00679

Scheller, E. L., Razzell Hollis, J., Cardarelli, E. L., Steele, A., Beegle, L. W., Bhartia, R., et al. (2022). Aqueous alteration processes in Jezero crater, Mars—Implications for organic geochemistry. *Science*, *378*(6624), 1105–1110. https://doi.org/10.1126/science.abo5204

Schmid, T., Jungnickel, R., & Dariz, P. (2020). Insights into the $CaSO_4$–H_2O system: A Raman-spectroscopic study. *Minerals*, *10*(2), 115. https://doi.org/10.3390/min10020115

Sharma, S., Roppel, R. D., Murphy, A. E., Beegle, L. W., Bhartia, R., Steele, A., et al. (2023). Diverse organic-mineral associations in Jezero crater, Mars. *Nature*, *619*(7971), 1–9. https://doi.org/10.1038/s41586-023-06143-z

Sheppard, R. Y., Milliken, R. E., & Robertson, K. M. (2022). Presence of clay minerals can obscure spectral evidence of Mg sulfates: Implications for orbital observations of Mars. *Icarus*, *383*, 115083. https://doi.org/10.1016/j.icarus.2022.115083

Siebach, K. L., Nachon, M., Sholes, S. F., Sun, V. Z., Del Sesto, T., Weiss, B. P., et al. (2023). Overview of perseverance's upper fan campaign. In *Paper presented at the AGU annual meeting 2023, P41E-3232*. Retrieved from https://agu.confex.com/agu/fm23/meetingapp.cgi/Paper/1325383

Siljeström, S., Czaja, A. D., Corpolongo, A., Berger, E. L., Li, A. Y., Cardarelli, E., et al. (2024). Evidence of sulfate-rich fluid alteration in Jezero Crater floor, Mars. *Journal of Geophysical Research: Planets*, *129*(1), e2023JE007989. https://doi.org/10.1029/2023JE007989

Smith, R. J., McLennan, S. M., Sutter, B., Rampe, E. B., Dehouck, E., Siebach, K. L., et al. (2022). X-ray amorphous sulfur-bearing phases in sedimentary rocks of Gale Crater, Mars. *Journal of Geophysical Research: Planets*, *127*(5), e2021JE007128. https://doi.org/10.1029/2021JE007128

Squyres, S. W., Arvidson, R. E., Bell, J. F., Calef, F., Clark, B. C., Cohen, B. A., et al. (2012). Ancient impact and aqueous processes at endeavour crater, Mars. *Science*, *336*(6081), 570–576. https://doi.org/10.1126/science.1220476

Stack, K. M., Ives, L. R. W., Gupta, S., Lamb, M. P., Tebolt, M., Caravaca, G., et al. (2024). Sedimentology and stratigraphy of the Shenandoah formation, western fan, Jezero Crater, Mars. *Journal of Geophysical Research: Planets*, *129*(2), e2023JE008187. https://doi.org/10.1029/2023JE008187

Stack, K. M., Williams, N. R., Calef, F., Sun, V. Z., Williford, K. H., Farley, K. A., et al. (2020). Photogeologic map of the perseverance rover field site in Jezero Crater constructed by the Mars 2020 science team. *Space Science Reviews*, *216*(8), 127. https://doi.org/10.1007/s11214-020-00739-x

Sutter, B., McAdam, A. C., Mahaffy, P. R., Ming, D. W., Edgett, K. S., Rampe, E. B., et al. (2017). Evolved gas analyses of sedimentary rocks and eolian sediment in Gale Crater, Mars: Results of the Curiosity rover's sample analysis at Mars instrument from Yellowknife Bay to the Namib Dune. *Journal of Geophysical Research: Planets*, *122*(12), 2574–2609. https://doi.org/10.1002/2016JE005225

Talla, D., & Wildner, M. (2019). Investigation of the kieserite–szomolnokite solid-solution series, $(Mg, Fe)SO_4{\cdot}H_2O$, with relevance to Mars: Crystal chemistry, FTIR, and Raman spectroscopy under ambient and martian temperature conditions. *American Mineralogist*, *104*(12), 1732–1749. https://doi.org/10.2138/am-2019-6983

Tarnas, J. D., Mustard, J. F., Lin, H., Goudge, T. A., Amador, E. S., Bramble, M. S., et al. (2019). Orbital identification of hydrated silica in Jezero Crater, Mars. *Geophysical Research Letters*, *46*(22), 12771–12782. https://doi.org/10.1029/2019GL085584

Thomas, N. H., Ehlmann, B. L., Anderson, D. E., Clegg, S. M., Forni, O., Schröder, S., et al. (2018). Characterization of hydrogen in basaltic materials with laser-induced breakdown spectroscopy (LIBS) for application to MSL ChemCam data. *Journal of Geophysical Research: Planets*, *123*(8), 1996–2021. https://doi.org/10.1029/2017JE005467

Thomas, N. H., Ehlmann, B. L., Rapin, W., Rivera-Hernández, F., Stein, N. T., Frydenvang, J., et al. (2020). Hydrogen variability in the Murray formation, Gale Crater, Mars. *Journal of Geophysical Research: Planets*, *125*(9), e2019JE006289. https://doi.org/10.1029/2019JE006289

Thorpe, M. T., Bristow, T. F., Rampe, E. B., Tosca, N. J., Grotzinger, J. P., Bennett, K. A., et al. (2022). Mars science laboratory CheMin data from the Glen Torridon region and the significance of lake-groundwater interactions in interpreting mineralogy and sedimentary history. *Journal of Geophysical Research: Planets*, *127*(11), e2021JE007099. https://doi.org/10.1029/2021JE007099

Tice, M. M., Hurowitz, J. A., Allwood, A. C., Jones, M. W. M., Orenstein, B. J., Davidoff, S., et al. (2022). Alteration history of Seitah formation rocks inferred by PIXL X-ray fluorescence, X-ray diffraction, and multispectral imaging on Mars. *Science Advances*, *8*(47), eabp9084. https://doi.org/10.1126/sciadv.abp9084

Tlili, M. M., Ben Amor, M., Gabrielli, C., Joiret, S., Maurin, G., & Rousseau, P. (2002). Characterization of $CaCO_3$ hydrates by micro-Raman spectroscopy. *Journal of Raman Spectroscopy*, *33*(1), 10–16. https://doi.org/10.1002/jrs.806

Tosca, N. J., & McLennan, S. M. (2006). Chemical divides and evaporite assemblages on Mars. *Earth and Planetary Science Letters*, *241*(1), 21–31. https://doi.org/10.1016/j.epsl.2005.10.021

Tutolo, B. M., Hausrath, E. M., Rampe, E. B., Bristow, T. F., Downs, R. T., Kite, E., et al. (2024). In situ evidence for an active carbon cycle on ancient Mars. In *Paper presented at the 55th lunar and planetary science conference (LPSC)*. Retrieved from https://www.hou.usra.edu/meetings/lpsc2024/pdf/1564.pdf

Uckert, K. (2022). Nasa/loupe: LoupeV5.1.5 (LoupeV5.1.5a). *Zenodo*. https://doi.org/10.5281/ZENODO.7062998

Vaniman, D. T., Bish, D. L., Chipera, S. J., Fialips, C. I., William Carey, J., & Feldman, W. C. (2004). Magnesium sulphate salts and the history of water on Mars. *Nature*, *431*(7009), 663–665. https://doi.org/10.1038/nature02973

Vaniman, D. T., Bish, D. L., Ming, D. W., Bristow, T. F., Morris, R. V., Blake, D. F., et al. (2014). Mineralogy of a mudstone at Yellowknife Bay, Gale Crater, Mars. *Science*, *343*(6169), 1243480. https://doi.org/10.1126/science.1243480

Vaniman, D. T., & Chipera, S. J. (2006). Transformations of Mg- and Ca-sulfate hydrates in Mars regolith. *American Mineralogist*, *91*(10), 1628–1642. https://doi.org/10.2138/am.2006.2092

Vaniman, D. T., Martínez, G. M., Rampe, E. B., Bristow, T. F., Blake, D. F., Yen, A. S., et al. (2018). Gypsum, bassanite, and anhydrite at Gale crater, Mars. *American Mineralogist*, *103*(7), 1011–1020. https://doi.org/10.2138/am-2018-6346

Vasavada, A. R., Piqueux, S., Lewis, K. W., Lemmon, M. T., & Smith, M. D. (2017). Thermophysical properties along Curiosity's traverse in Gale crater, Mars, derived from the REMS ground temperature sensor. *Icarus*, *284*, 372–386. https://doi.org/10.1016/j.icarus.2016.11.035

Virtanen, P., Gommers, R., Oliphant, T. E., Haberland, M., Reddy, T., Cournapeau, D., et al. (2020). Scipy 1.0: Fundamental algorithms for scientific computing in python. *Nature Methods*, *17*(3), 261–272. https://doi.org/10.1038/s41592-019-0686-2

Walrafen, G. E., Yang, W.-H., Chu, Y. C., & Hokmabadi, M. S. (1996). Raman OD-stretching overtone spectra from liquid D2O between 22 and 152°C. *The Journal of Physical Chemistry*, *100*(4), 1381–1391. https://doi.org/10.1021/jp952134i

Wang, A., Freeman, J. J., Chou, I.-M., & Jolliff, B. L. (2011). Stability of Mg-sulfates at −10°C and the rates of dehydration/rehydration processes under conditions relevant to Mars. *Journal of Geophysical Research*, *116*(E12), E12006. https://doi.org/10.1029/2011JE003818

Wang, A., Freeman, J. J., & Jolliff, B. L. (2009). Phase transition pathways of the hydrates of magnesium sulfate in the temperature range 50°C to 5°C: Implication for sulfates on Mars. *Journal of Geophysical Research*, *114*(E4), E04010. https://doi.org/10.1029/2008JE003266

Wang, A., Freeman, J. J., & Jolliff, B. L. (2015). Understanding the Raman spectral features of phyllosilicates. *Journal of Raman Spectroscopy*, *46*(10), 829–845. https://doi.org/10.1002/jrs.4680

Wang, A., Freeman, J. J., Jolliff, B. L., & Chou, I.-M. (2006). Sulfates on Mars: A systematic Raman spectroscopic study of hydration states of magnesium sulfates. *Geochimica et Cosmochimica Acta*, *70*(24), 6118–6135. https://doi.org/10.1016/j.gca.2006.05.022

Wang, A., Jolliff, B. L., Liu, Y., & Connor, K. (2016). Setting constraints on the nature and origin of the two major hydrous sulfates on Mars: Monohydrated and polyhydrated sulfates. *Journal of Geophysical Research: Planets*, *121*(4), 678–694. https://doi.org/10.1002/2015JE004889

Wei, J., Wang, A., Lambert, J. L., Wettergreen, D., Cabrol, N., Warren-Rhodes, K., & Zacny, K. (2015). Autonomous soil analysis by the Mars micro-beam Raman spectrometer (MMRS) on-board a rover in the Atacama Desert: A terrestrial test for planetary exploration. *Journal of Raman Spectroscopy*, *46*(10), 810–821. https://doi.org/10.1002/jrs.4656

Wiens, R. C., Maurice, S., Robinson, S. H., Nelson, A. E., Cais, P., Bernardi, P., et al. (2021). The SuperCam instrument suite on the NASA Mars 2020 rover: Body unit and combined system tests. *Space Science Reviews*, *217*(1), 4. https://doi.org/10.1007/s11214-020-00777-5

Wiens, R. C., Udry, A., Beyssac, O., Quantin-Nataf, C., Mangold, N., Cousin, A., et al. (2022). Compositionally and density stratified igneous terrain in Jezero crater, Mars. *Science Advances*, *8*(34), eabo3399. https://doi.org/10.1126/sciadv.abo3399

Wogsland, B. V., Minitti, M. E., Kah, L. C., Yingst, R. A., Abbey, W., Bhartia, R., et al. (2023). Science and science-enabling activities of the SHERLOC and WATSON imaging systems in Jezero Crater, Mars. *Earth and Space Science*, *10*(11), e2022EA002544. https://doi.org/10.1029/2022EA002544